Cell Genomics

Resource

A systems biology approach uncovers novel disease mechanisms in age-related macular degeneration

Graphical abstract

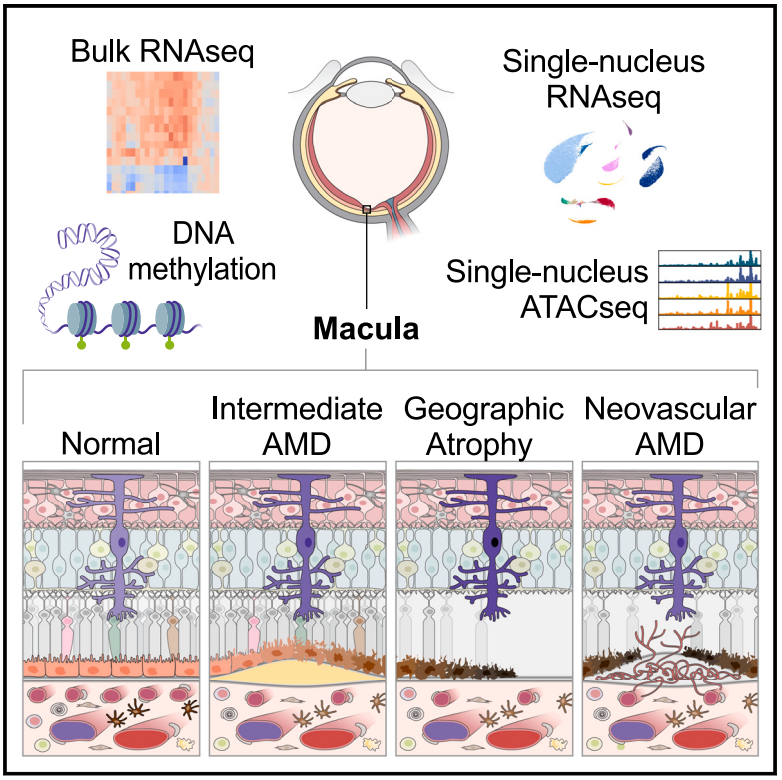

Highlights

- Bulk transcriptome and DNA methylation from RPE/choroid of phenotyped AMD eyes
- Single-nucleus RNA-seq and ATAC-seq from retina, RPE, and choroid of control and AMD eyes
- Single-nucleus RNA-seq and ATAC-seq prioritized putative causal genes at AMD GWAS loci
- Integrative analysis identified WNT pathway regulators *FRZB* and *TLE2* as AMD genes

Authors

Luz D. Orozco, Leah A. Owen, Jeffrey Hofmann, ..., Brian L. Yaspan, Hsu-Hsin Chen, Margaret M. DeAngelis

Correspondence

orozcogl@gene.com (L.D.O.), chen.hsuhsin@gene.com (H.-H.C.), mmdeange@buffalo.edu (M.M.D.)

In brief

There is limited information on molecular changes in age-related macular degeneration (AMD), a leading cause of blindness. Orozco et al. built expression and epigenetic atlases of control and phenotyped AMD eyes at both bulk-tissue and single-cell levels. Their integrative analysis of these data unveiled genes and pathways driving disease.

Orozco et al., 2023, Cell Genomics *3*, 100302
June 14, 2023
https://doi.org/10.1016/j.xgen.2023.100302

CellPress

Cell Genomics

CellPress
OPEN ACCESS

Resource

A systems biology approach uncovers novel disease mechanisms in age-related macular degeneration

Luz D. Orozco,[1,17,18,*] Leah A. Owen,[2,3,4,5] Jeffrey Hofmann,[6] Amy D. Stockwell,[7] Jianhua Tao,[6] Susan Haller,[6] Vineeth T. Mukundan,[1] Christine Clarke,[1] Jessica Lund,[8] Akshayalakshmi Sridhar,[9] Oleg Mayba,[1] Julie L. Barr,[5,10] Rylee A. Zavala,[5] Elijah C. Graves,[5] Charles Zhang,[5] Nadine Husami,[5,11] Robert Finley,[5] Elizabeth Au,[5] John H. Lillvis,[5,12] Michael H. Farkas,[5,10,11,12] Akbar Shakoor,[2] Richard Sherva,[13] Ivana K. Kim,[14] Joshua S. Kaminker,[1] Michael J. Townsend,[9] Lindsay A. Farrer,[13] Brian L. Yaspan,[7] Hsu-Hsin Chen,[9,16,17,*] and Margaret M. DeAngelis[2,3,5,10,15,16,17,*]

[1]Department of Bioinformatics and Computational Biology, Genentech, South San Francisco, CA 94080, USA
[2]Department of Ophthalmology and Visual Sciences, University of Utah School of Medicine, The University of Utah, Salt Lake City, UT 84132, USA
[3]Department of Population Health Sciences, University of Utah School of Medicine, The University of Utah, Salt Lake City, UT 84132, USA
[4]Department of Obstetrics and Gynecology, University of Utah School of Medicine, The University of Utah, Salt Lake City, UT 84132, USA
[5]Department of Ophthalmology, Ross Eye Institute, Jacobs School of Medicine and Biomedical Sciences, State University of New York, University at Buffalo, Buffalo, NY 14203, USA
[6]Department of Pathology, Genentech, South San Francisco, CA 94080, USA
[7]Department of Human Genetics, Genentech, South San Francisco, CA 94080, USA
[8]Departments of Microchemistry, Proteomics and Lipidomics, Genentech, South San Francisco, CA 94080, USA
[9]Department of Human Pathobiology & OMNI Reverse Translation, Genentech, South San Francisco, CA 94080, USA
[10]Neuroscience Graduate Program, Jacobs School of Medicine and Biomedical Sciences, State University of New York, University at Buffalo, Buffalo, NY 14203, USA
[11]Department of Biochemistry, Jacobs School of Medicine and Biomedical Sciences, State University of New York, University at Buffalo, Buffalo, NY 14203, USA
[12]Veterans Administration Western New York Healthcare System, Buffalo, NY 14212, USA
[13]Department of Medicine, Biomedical Genetics, Boston University School of Medicine, Boston, MA 02118, USA
[14]Retina Service, Massachusetts Eye & Ear, Department of Ophthalmology, Harvard Medical School, Boston, MA 02114, USA
[15]Genetics, Genomics and Bioinformatics Graduate Program, Jacobs School of Medicine and Biomedical Sciences, State University of New York, University at Buffalo, Buffalo, NY 14203, USA
[16]These authors contributed equally
[17]Senior author
[18]Lead contact
*Correspondence: orozcogl@gene.com (L.D.O.), chen.hsuhsin@gene.com (H.-H.C.), mmdeange@buffalo.edu (M.M.D.)
https://doi.org/10.1016/j.xgen.2023.100302

SUMMARY

Age-related macular degeneration (AMD) is a leading cause of blindness, affecting 200 million people worldwide. To identify genes that could be targeted for treatment, we created a molecular atlas at different stages of AMD. Our resource is comprised of RNA sequencing (RNA-seq) and DNA methylation microarrays from bulk macular retinal pigment epithelium (RPE)/choroid of clinically phenotyped normal and AMD donor eyes (n = 85), single-nucleus RNA-seq (164,399 cells), and single-nucleus assay for transposase-accessible chromatin (ATAC)-seq (125,822 cells) from the retina, RPE, and choroid of 6 AMD and 7 control donors. We identified 23 genome-wide significant loci differentially methylated in AMD, over 1,000 differentially expressed genes across different disease stages, and an AMD Müller state distinct from normal or gliosis. Chromatin accessibility peaks in genome-wide association study (GWAS) loci revealed putative causal genes for AMD, including *HTRA1* and *C6orf223*. Our systems biology approach uncovered molecular mechanisms underlying AMD, including regulators of WNT signaling, *FRZB* and *TLE2*, as mechanistic players in disease.

INTRODUCTION

Age-related macular degeneration (AMD) is a progressive neurodegenerative condition and a leading cause of blindness, affecting an estimated 200 million people worldwide.[1] Early to intermediate AMD is characterized by lipid-protein deposits termed drusen in the Bruch's membrane, a multilayered structure including the basement membrane of the retinal pigment epithelium (RPE). Two presentations of advanced AMD lead to severe loss of central vision: the "wet" form is characterized by subretinal neovascularization (neovascular [NEO]) with subsequent loss of retinal function, and the "dry" phenotype

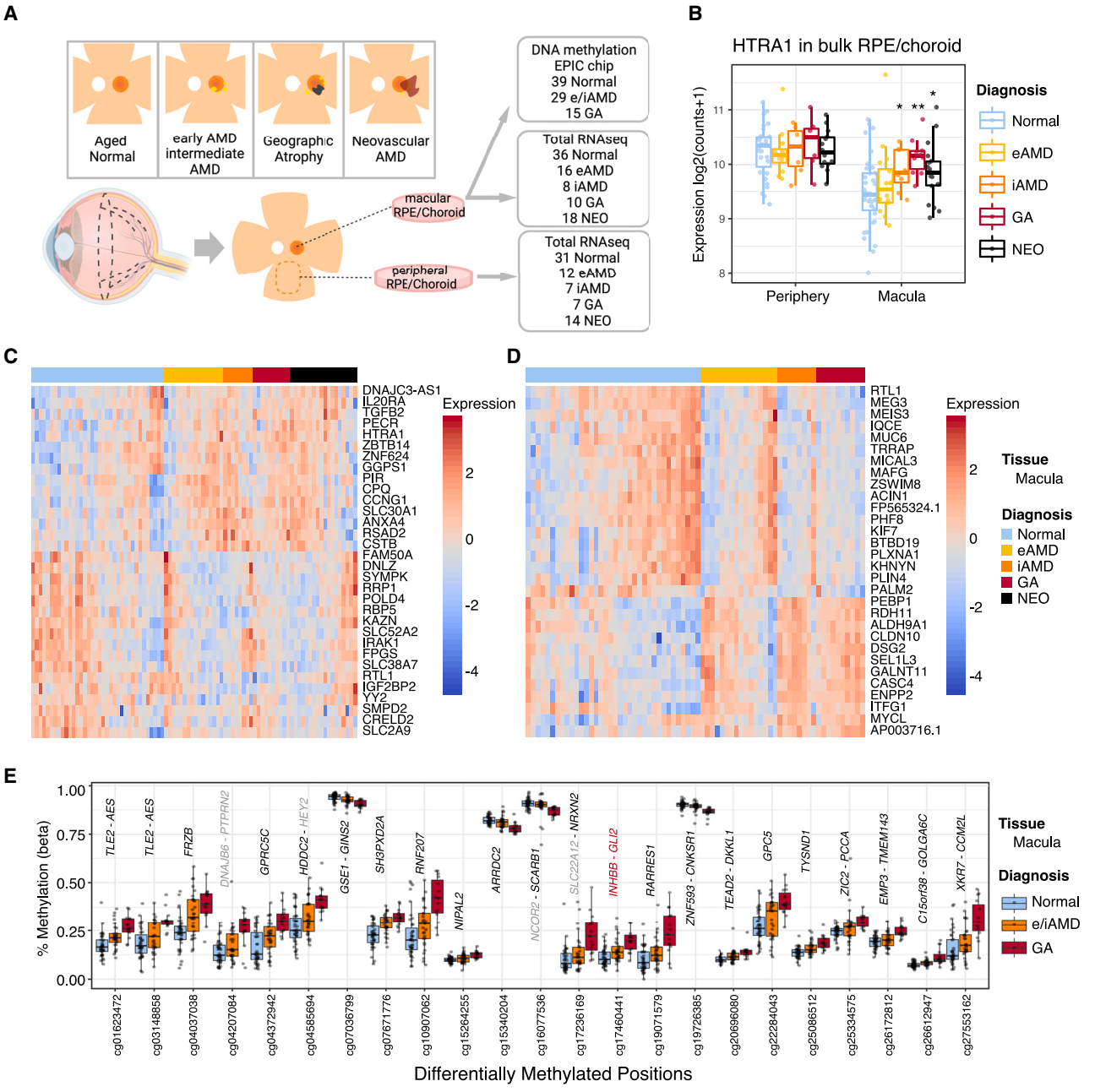

(legend on next page)

(geographic atrophy [GA]) is characterized by patchy degeneration of the RPE and the photoreceptors. Notably, both advanced presentations can co-occur in the same patient, indicating that the progression mechanisms are not mutually exclusive.[2] Anti-VEGF therapeutics are effective for NEO advanced AMD, but treatment options for the dry forms of AMD are still limited.

AMD is a multifactorial disease driven by both genetic and environmental risk factors. Many of the latter are shared with other complex chronic conditions associated with aging.[3–5] In the past decade, large genome-wide association studies (GWAS) across genetic ancestries have unveiled the heritable components of disease risk,[6,7] highlighting the complement pathway and the *ARMS2-HTRA1* locus, which make up the basis of the vast majority of GA clinical trials. The AMD consortium reported that these loci are also associated with increased risk of progression into late stages of the disease.[8,9] While multiple cell types, ocular and systemic, play a role in the development of AMD, the cell-type expression profiles of AMD candidate genes,[10] the histopathology of drusen and AMD lesions, choriocapillaris dropout in disease tissues,[11] and the emergence of RPE cell replacement as a therapeutic strategy for AMD[12–14] all indicate the RPE and choroid as the initial sites of AMD pathogenesis.

A systems biology approach of the molecular and genetic aspects of disease holds particular promise for elucidating the pathophysiological mechanisms of AMD, which are essential for disease intervention and prevention.[15,16] These multipronged efforts have been limited, as published studies have largely employed tissues from animal models,[17] *in-vitro*-derived retinal organoids,[18,19] and induced RPE cells from patient-derived induced pluripotent stem cells (iPSCs).[20] While these studies are invaluable in furthering our understanding of ocular biology, both *in vitro* and animal models have not been able to fully recapitulate human pathology. The paucity of AMD molecular datasets, especially of the RPE/choroid, is partly due to the lack of well-characterized disease and normal human macular tissue with rigorous postmortem intervals (death-to-preservation time). Furthermore, studies examining ocular tissues in bulk or single cells[21–25] have been heavily skewed toward retinal populations, while few have included the RPE and choroidal cell types,[10,26,27] which are crucial players in the development and progression of AMD.

Here, we present a molecular analysis of human macular tissues from well-characterized donor eyes including the retina, RPE, and choroid, with phenotypes ranging from normal to early and intermediate AMD, GA AMD, and NEO AMD. Our newly generated data include (1) DNA methylation from bulk macular RPE/choroid, (2) total RNA sequencing (RNA-seq) from bulk RPE/choroid from the macula and periphery, (3) single-nucleus transcriptomics, and (4) single-nucleus chromatin accessibility from the retina, RPE, and choroid. Our results reveal cell type-specific gene expression, genome-wide significant differences in DNA methylation, and gene expression changes at different stages of AMD specific to the macula. Integrative analyses of our data, including chromatin accessibility peak-to-gene correlation and rare variant burden tests in patient cohorts with GA, highlighted the canonical WNT signaling pathway, and in particular *FRZB/SFRP3* and *TLE2* genes, as a novel component of GA AMD. Our work has revealed putative causal genes and pathways underlying genetic risk for AMD and underscores the power of a systems biology approach for elucidating mechanisms driving AMD.

RESULTS

Overview of AMD molecular data

To uncover molecular changes in AMD, we generated bulk-tissue and single-cell transcriptomics and epigenomics data from a large panel of AMD human donor eyes. At the bulk-tissue level, we profiled the transcriptomes of the RPE/choroid using both macular and peripheral regions at different stages of AMD (n = 85 unique donors). We phenotyped these donor eyes using clinical AREDS criteria based on postmortem retinal imaging.[2] All AMD phenotypes were represented, including normal control (AREDS 0/1), early AMD (eAMD/AREDS2), intermediate AMD (iAMD/AREDS3), and both types of advanced stages, GA and NEO AMD (Figure 1A; Table S1, ST1A). We also profiled DNA methylation in bulk macular RPE/choroid from normal, eAMD/iAMD, and GA donors (n = 82 unique donors after quality control [QC], 19 are from the same samples as RNA-seq). At the single-cell level, we profiled the transcriptomes using single-nucleus RNA-seq (sNuc-seq), and genome-wide chromatin accessibility using single-nucleus assay for transposase-accessible chromatin-seq (snATAC-seq) from posterior eye tissue including retina, RPE, and choroid (7 control and 6 AMD donors, not phenotyped).

We identified gene expression and DNA methylation differences between control and AMD donors in bulk tissue. At the single-cell level, we compared gene expression and chromatin accessibility between control and advanced AMD. We integrated our expression and epigenetic data with GWAS loci for AMD risk through correlation between chromatin accessibility

Figure 1. Characterization of bulk macular RPE/choroid tissues

(A) Schematic representation of phenotyped bulk eye tissue analyses. Created with Biorender.com.

(B) Normalized *HTRA1* gene expression in bulk RNA-seq. *FDR < 0.05, **FDR < 0.05, and fold change > 1.5; see Table S1 (ST1B). Boxplot is drawn from 25th to 75th percentiles, horizontal bars are medians, and whiskers show ranges.

(C and D) Heatmap of top DEGs in bulk RNA-seq from macular RPE/choroid for (C) pairwise comparisons of normal vs. each AMD stage, and (D) linear analysis of normal and dry AMD.

(E) DMPs between normal and GA. Genes <100 kb from the cytosine are in black, genes located 100 kB to 1 Mb away are in gray, and genes labeled in red are published AMD GWAS candidates.

(F and G) Venn diagrams of DEGs for (F) normal vs. GA and normal vs. NEO and (G) normal vs. eAMD, normal vs. iAMD, and normal vs. GA. See Table S1 (ST1B).

(H) Venn diagram of macular RPE/choroid DEGs in normal vs. GA, DEGs in normal vs. iAMD, and closest genes to DMP in normal vs. GA.

See also Figure S1.

Table 1. Summary of bulk RPE/choroid RNA-seq and methylation

Differential expression	Tissue	Genes FDR <5%	Genes FDR <5% and fold change >1.5 (up or down)
Normal vs. early AMD in macula	macula RPE/choroid	1,807	408
Normal vs. intermediate AMD in macula	macula RPE/choroid	1,792	886
Normal vs. geographic atrophy in macula	macula RPE/choroid	1,742	719
Normal vs. early AMD plus intermediate AMD plus geographic atrophy in macula (pooled dry AMD)	macula RPE/choroid	4,796	1,001
Normal vs. neovascular AMD in macula	macula RPE/choroid	2,882	696
Normal vs. early AMD in periphery	periphery RPE/choroid	0	0
Normal vs. intermediate AMD in periphery	periphery RPE/choroid	0	0
Normal vs. geographic atrophy in periphery	periphery RPE/choroid	0	0
Normal vs. early AMD plus intermediate AMD plus geographic atrophy in periphery (pooled dry AMD)	periphery RPE/choroid	0	0
Normal vs. neovascular AMD in periphery	periphery RPE/choroid	0	0
Periphery vs. macula in all samples	periphery vs. macula	8,300	1,714
Linear analysis for dry AMD in macula	macula RPE/choroid	2,383	17
Linear analysis for dry AMD in periphery	periphery RPE/choroid	4	0
Linear analysis for age in macula (normal controls)	macula RPE/choroid	1,514	0
Linear analysis for age in periphery (normal controls)	periphery RPE/choroid	1	0
Differential methylation	tissue	DMP FDR <5%	
Normal vs. geographic atrophy	macula RPE/choroid	22	–
Linear analysis across all dry AMD	macula RPE/choroid	1	–

at specific loci and expression of nearby genes. In addition to published GWAS, we leveraged existing whole-genome sequencing (WGS) data from the lampalizumab clinical trials for GA in a rare variant burden test for specific genes of interest. Finally, we incorporated public gene expression datasets into our analysis, including bulk retina and RPE/choroid RNA-seq (each from the macula or periphery) of control and AMD eyes without phenotyping[10] and single-cell RNA-seq from human foveal and peripheral retina that included RPE.[18]

Differential expression in bulk RPE/choroid from phenotyped donors

We performed differential gene expression analysis in bulk RNA-seq from RPE/choroid between normal controls and different stages of AMD for both macular and peripheral regions. We found differentially expressed genes (DEGs; false discovery rate [FDR] < 5% and fold change > 1.5 up or down) only in macular, but not peripheral, tissues (Table 1). We found 408 DEGs in normal vs. eAMD, 886 in iAMD, 719 in GA, 696 in NEO, and 1,001 in normal vs. all pooled dry AMD (eAMD, iAMD, and GA). In a linear analysis using the dry AMD stage as the predictor, we found 2,383 genes with FDR <5%. Importantly, there were no DEGs in the periphery between normal and AMD eyes at any stage. For example, *HTRA1*, a top candidate gene for genetic risk for AMD, showed significantly higher expression in iAMD, GA, and NEO in the macular RPE/choroid (Figure 1B).

Using only normal controls, we identified age-related gene expression changes independently of AMD, with 1,514 genes changing with age in the macula (FDR < 5%), but only one in the periphery (Table 1). In both regions, the effect of age on gene expression was modest, and none of the genes with FDR <5% showed fold change above 1.5. Consistent with previous transcriptomics studies of RPE/choroid, we identified 1,714 DEGs between macular and peripheral eye regions (Figure S1C; Table S1, ST1B). Top regional DEGs were corroborated by the single-cell dataset in Cowan et al.,[18] including *SLIT2* (enriched in foveal RPE), *COL9A2* (enriched in peripheral RPE), and *SHOX* (enriched in peripheral fibroblasts). The top DEGs are shown in Figures 1C and 1D. The complete list of DEGs is in Table S1 (ST1B-C).

Genome-wide DNA methylation profiles in phenotyped macular RPE/choroid

We profiled DNA methylation levels in macular RPE/choroid tissues using the Illumina 850K EPIC BeadChips (Figure S1D-E). We compared methylation levels across normal controls, eAMD/iAMD, and GA groups to identify differentially methylated positions (DMPs) at individual CpG cytosines and differentially methylated regions (DMRs). While we did not find significant DMRs, we identified 22 DMPs in control vs. GA and 1 DMP in a linear analysis of all dry AMD groups at genome-wide significance (Figure 1E; Table 1; Table S1, ST1E). In general, the average methylation levels of eAMD/iAMD samples fell in between the normal controls and GA samples in all 23 DMPs, of which 19 showed an increase in methylation with disease progression. We annotated the nearest genes to DMPs based on

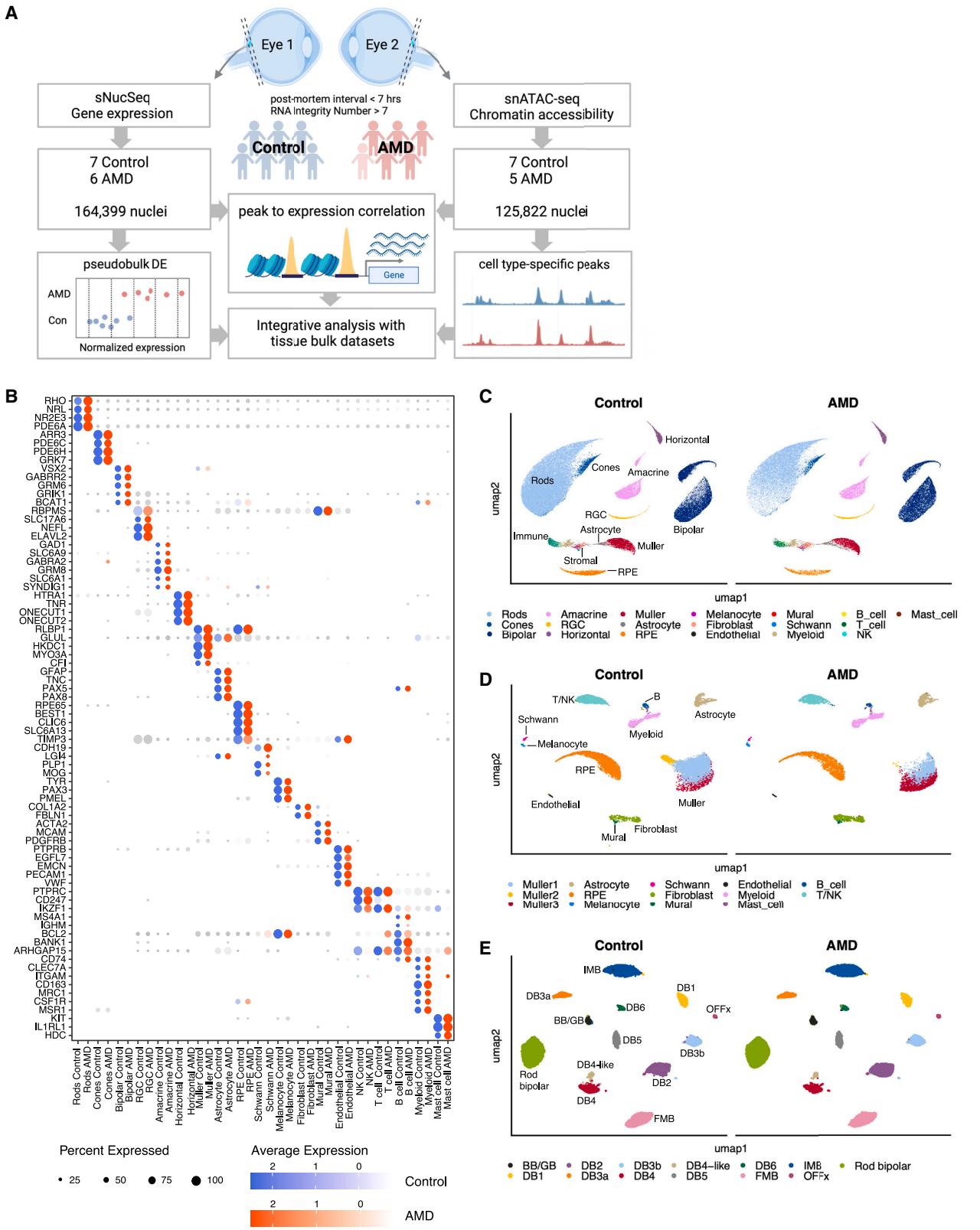

(legend on next page)

physical proximity, resulting in 35 nearest genes, including *GLI2*, a GWAS candidate for eAMD.[28] Intersecting the genes annotated to DMPs with our bulk differential expression analysis highlighted a small number of genes (Figures 1F–1H): *FRZB* and *TLE2* were DE and differentially methylated in normal vs. GA, and *SH3PXD2A* was DE in normal vs. iAMD and differentially methylated in the linear methylation analysis of dry AMD. Overall, our results suggest that epigenetic differences accumulate in the disease state, where differences emerge at the iAMD stage, and become more pronounced as the disease advances to GA. The relatively small number of DMPs is consistent with previous studies that found methylation marks to be largely stable relative to gene expression and primarily variable between cell types.

sNuc-seq from control and AMD human retina, RPE, and choroid

Our sNuc-seq on retina, RPE, and choroid yielded 164,399 nuclei from 7 control and 6 advanced AMD donors (without phenotyping; Figures 2A and S2A-C). We identified all major cell types (Figures 2B, 2C, and S2D; Table S1, ST1F) and achieved subtype resolution (Figures 2D, 2E, and S2E–S2G) based on the expression profiles.[10,17,29] We observed no differences in cell type-specific markers (Figure 2B) between control and AMD. Likewise, the nuclei clustered primarily by cell type and not by disease status (Figure 2C). We did not observe clustering by disease in any cell types including photoreceptors, horizontal cells, amacrine cells, retinal ganglion cells (RGCs), or bipolar cells (Figures 2E and S2E–S2G). In contrast, we observed a significant shift in the proportion of AMD cells across the Müller clusters (Fisher's exact p = 5.0E−4; Figure 2D, see below).

To uncover AMD-related gene expression changes, we performed pseudo-bulk differential expression analysis for each major cell type. We found few significant DEGs (FDR < 5%), likely due to the small number of donors. However, we identified genes showing suggestive differences between control and AMD and highlight the Müller, RPE, rod, and fibroblast top genes in Figures 3A–3F and S3A–S3E. The sNuc-seq pseudo-bulk analysis showed limited overlap with DEGs in our bulk RPE/choroid RNA-seq data. This is unsurprising given the complementary nature of the bulk and single-cell approaches, where the bulk approach had higher sensitivity and power and the single-cell approach resolved cell type-specific signals. The top ranked gene lists are in Table S1 (ST1G).

Among the top 20 RPE pseudo-bulk DEGs are *MERTK*, *DOCK3*, *STAM*, and *HTRA1* (Table S1, ST1G). *MERTK* is an essential gene for phagocytosis and was lower in AMD (Figure 3C), suggesting decreased cellular function in disease. *MERTK* shows much higher expression in macrophages, which likely obscures the RPE signal in bulk data. Similarly, *DOCK3* is highly expressed in RPE and melanocytes, and the melanocyte signal may mask the RPE-specific changes in the bulk data. *STAM* is a rare example that showed increased expression in disease both in sNuc-seq (RPE) and bulk RPE/choroid. We also found a small set of genes with increased expression in AMD fibroblasts (Figures 3D and S3E), which may reflect the disease fibrotic response. *RBP3*, an essential gene for shuttling retinoids in the visual cycle, was higher in AMD rods compared with controls (Figure S3C). This trend was not seen in published retina bulk transcriptomes[10,30] and could be attributed to differential nuclear retention of the transcript.

We curated and examined 92 candidate genes from published GWAS loci for AMD.[6,7,28,31–39] Of these, 22 show none or negligible expression across all cell types, likely due to the effects of these genes in extraocular cell types or to sNuc-seq limit of detection. The vast majority of AMD GWAS candidate genes showed no differences in pseudo-bulk expression between control and AMD groups (Figure S3F).

Transcriptomic shift in AMD Müller glia

We resolved three clusters of Müller glia that appear to correspond to distinct cell states, referred to as basal (Müller cluster 1), AMD (Müller cluster 3), and gliotic (Müller cluster 2; Figure 2D). 62% of the basal Müller cluster were from controls, and 80% of the AMD Müller cluster were derived from AMD donors. Although Müller gliosis is a common feature in retinal diseases and injury, the AMD Müller cluster did not show higher expression of gliosis markers (Figures 3A and 3B) such as *GFAP*, *CCL2*, and *ICAM1*. The gliotic genes instead mark Müller cluster 2, composed predominantly of nuclei from one control donor, possibly due to an undiagnosed retinal inflammatory condition. We used pseudo-bulk DE analysis to identify top genes differentiating control and AMD Müller. These largely overlap with the marker genes that differentiate Müller clusters 1 (basal) and 3 (AMD), indicating that the cell state shift underlies transcriptomic changes associated with disease (Figure 3A). Among the top 20 pseudo-bulk DEGs in Müller glia are *ADAMTS18*, a causal gene for MMCAT (microcornea, myopic chorioretinal atrophy, and telecanthus), and *CLU*, a known drusen component which showed increased expression in AMD (Figures 3A, 3B, and 3E; Table S1, ST1G). Alpha B crystallin (*CRYAB*), another known drusen component, was highly expressed in Müller cells and trended higher in Müller cluster 3 (Figures 3A, 3B, and 3E). Additional marker genes differentiating the Müller clusters are listed in Table S1 ST1H.

To validate the AMD-related shift in Müller glia, we performed *in situ* hybridization (ISH) against *CRYAB* and *CLU* in macular sections with GA lesions (n = 3), eAMD/iAMD drusen (n = 3), and controls (n = 3). In controls, we found scattered *CRYAB*+ and *CLU*+ cells present in the inner nuclear layer (INL) and the ganglion cell layer (GCL) across macula and peripheral regions, consistent with enriched expression of both in Müller glia and

Figure 2. Single-nucleus RNA-seq of control and AMD donor eyes

(A) Overview of single-cell genomics workflow from human donor eyes.

(B) Dotplot of selected marker genes for major cell types. The color intensity is the normalized average expression, and the dot size represents the percentage of nuclei in each cell type with non-zero expression of that gene.

(C–E) Uniform manifold approximation and projection (UMAP) dimensionality reductions of expression in (C) major cell types, (D) non-neuronal cell types, and (E) bipolar cell subtypes.

See also Figure S2.

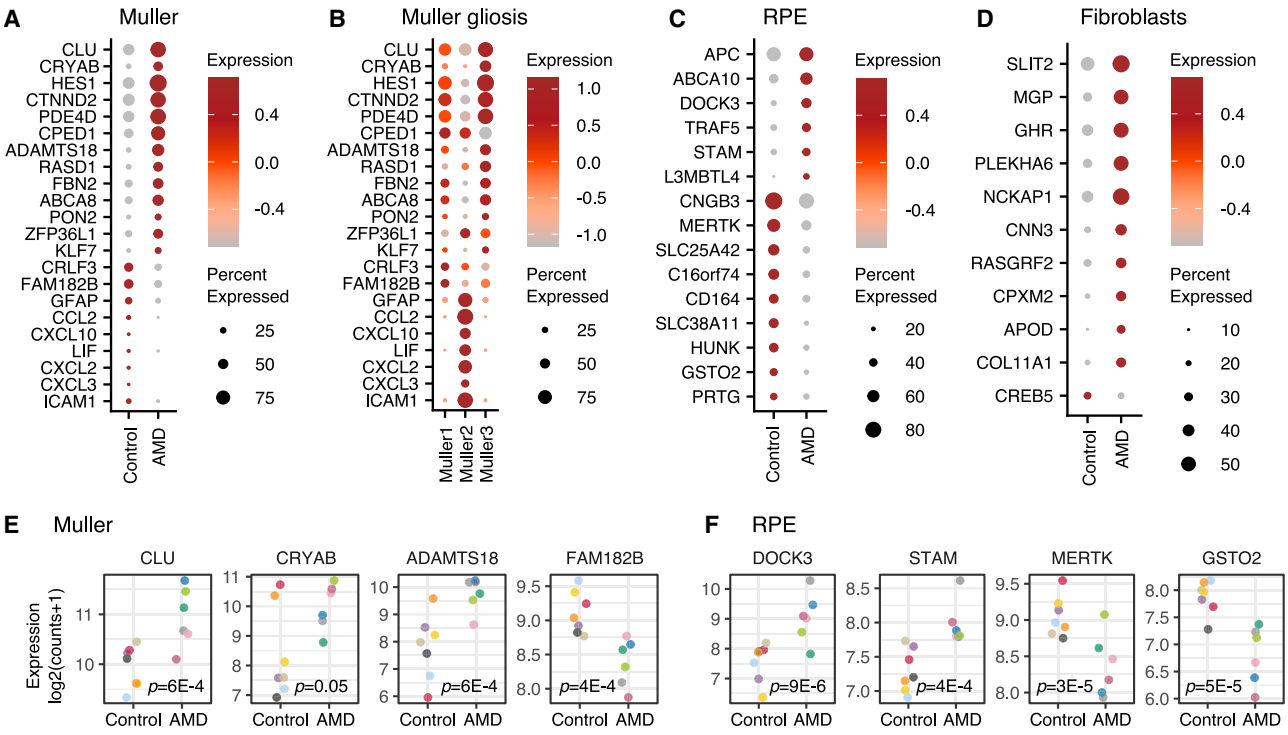

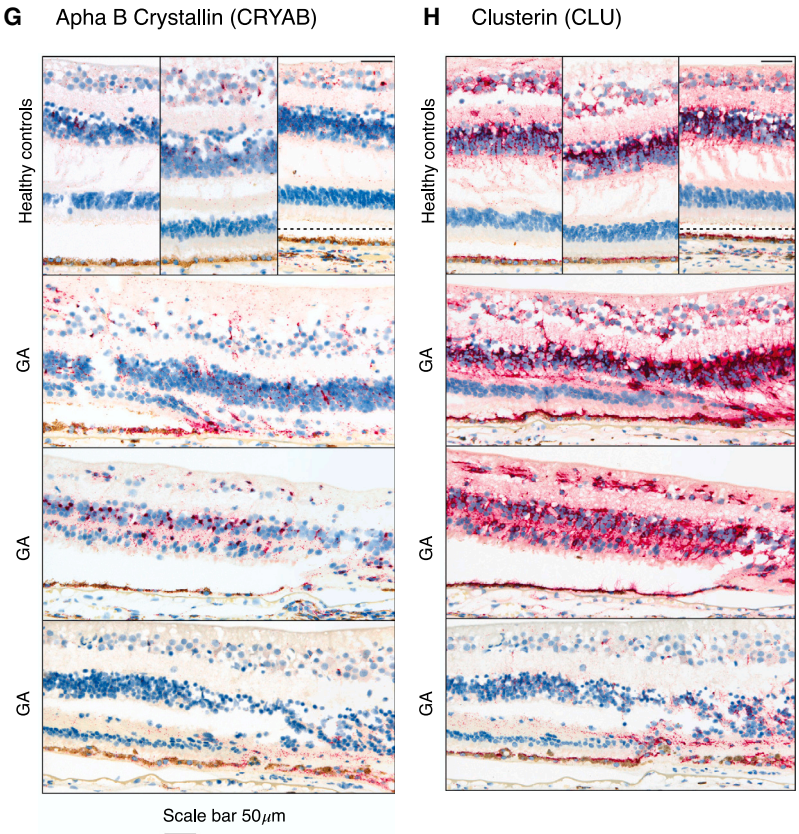

(legend on next page)

astrocytes (Figures 3G and 3H). For both genes, expression in eAMD/iAMD was similar to controls, including at sites of large basal laminar deposits and RPE dysmorphism. In GA, there was a striking increase in both *CRYAB* and *CLU* expression in lesion areas compared with non-lesional areas, eAMD/iAMD, or control retina. At the transitional zone surrounding GA lesions, *CRYAB*+ cells (likely displaced Müller glia) appear in the thinning outer nuclear layer (ONL; Figure 3G). RPE cells in the region also become *CRYAB*+; 3 of the 6 AMD donors, but none of the controls, also showed increased *CRYAB* expression in RPE sNuc-seq. We observed strong staining of *CRYAB*+ cells in completely atrophic and central lesional regions, including nests of pigmented cells and unpigmented cells, possibly a mixture of RPE and Müller glia. Similarly, *CLU*+ cells appear in the thinning ONL at lesion borders (Figure 3H) and at lesion centers as strongly positive patches, presumably composed of Müller glia and remaining RPE cells. Taken together, our ISH results confirmed the cell type expression patterns and our sNuc-seq observation that *CRYAB* and *CLU* were upregulated in AMD Müller glia.

Chromatin accessibility from contralateral eyes at cell subtype resolution

We performed snATAC-seq in control and AMD donor eyes and obtained 125,822 nuclei after QC (Figure 2A; STAR Methods), where the quality was largely comparable across donors, disease states, and cell types, with few exceptions (Figure S4A–S4F). Dimensional reduction and clustering based on chromatin accessibility resolved all major cell types (Figure 4A; Table S1, ST1I). The majority of cell type-specific accessibility peaks were distal and intronic instead of in promoter or exonic regions (Figure S4G). We subclustered major cell types and achieved further cell type and subtype resolution, which was largely on par with sNuc-seq, resolving non-neuronal cell types (Figure 4B), 13 bipolar subtypes (Figures 4C and 4D), horizontal H1 and H2 subtypes (data not shown), and cone M/L and S subtypes (Figure S4H), as well as multiple amacrine subtypes (Figure S4I). Integration of transcriptomics (sNuc-seq) and chromatin accessibility (snATAC-seq) identified all major cell types (Figures 4A, 4E, and 4F) and the 13 bipolar subtypes (Figure 4C). As an example, *DOK5* encodes a DB5 bipolar subtype-specific marker in sNuc-seq and also showed chromatin accessibility only in that cell type (Figure 4D). Consistent with studies in other tissues, our findings indicate that cell type-specific expression coincides with cell type-specific chromatin accessibility in the human retina, RPE, and choroid.

We performed differential accessibility analysis between control and AMD donors at the pseudo-bulk cell type level but found no genome-wide significant differences (FDR < 5%). Consistent with this, we observed no overt differences between control and AMD samples, at neither the cell type nor subtype levels (Figures 4A–4C, S4H, and S4I). In Müller glia, we did not detect a corresponding shift in chromatin accessibility as in sNuc-seq. Our results are in contrast to a previous bulk ATAC-seq study of control and AMD tissues[40] in which the disease state was associated with a global reduction of open chromatin. We did not replicate their findings either globally or at specific loci (Figure S4J). Importantly, our snATAC-seq dataset can resolve neuronal subtypes in the retina, and based on this observation, we expected to observe disease-related differences had there been a substantial shift in chromatin accessibility. One potential source of this discrepancy may be that nuclei of dead and dying cells in diseased tissues would contribute to bulk ATAC-seq but would not pass our snATAC-seq QC filters. Overall, our results indicate that chromatin accessibility is correlated primarily with cell type identity and not with disease state.

Using single-cell genomics to dissect AMD GWAS loci

To identify the ocular cell types most relevant to genetic risk of AMD, we applied SCAVENGE[41] to our snATAC-seq data, in conjunction with AMD GWAS risk loci.[6] SCAVENGE identified RPE and myeloid cells as the top disease-relevant cell types where the regulatory elements in GWAS loci are enriched in open chromatin regions (Figure 4G). This is consistent with our sNuc-seq observations here and in our previous work,[10] where a majority of GWAS candidate genes were expressed in RPE, immune, and choroidal cell types.

Identifying causal genes underlying GWAS loci is challenging,[42] in part because a large fraction of associations occur in intergenic regions, but also because each association can have multiple credible candidate genes due to linkage disequilibrium. Chromatin accessibility can also be used to prioritize candidate genes for a phenotype of interest. Correlation between cell type-specific chromatin accessibility and expression of nearby genes,[43] or "peak-to-gene" analysis, can highlight putative regulatory elements in GWAS loci. We performed peak-to-gene analysis across all cell types in our integrated sNuc-seq and snATAC-seq data and found 22 genes correlated with 7 AMD risk loci (Table 2; $R > 0.3$, FDR < 5%). In the *ARMS2-HTRA1* locus, the lead GWAS SNP overlaps an accessible peak in the RPE, which was in turn correlated with expression of *HTRA1* (Figure 4H; Table 2). In contrast, *ARMS2* expression was nearly undetectable in sNuc-seq, and neither *ARMS2* nor other neighboring genes showed correlation in this locus. This result, along with differential expression of *HTRA1* in disease

Figure 3. Pseudo-bulk differential expression from single-nucleus RNA-seq

(A–D) Dotplots showing marker gene expression in single-nucleus RNA-seq (sNuc-seq). The color intensity represents the *Z* score of gene expression, and the dot size represents the percentage of nuclei in each group with non-zero expression. Genes are from pseudo-bulk DE in (A) Müller glia, (B) genes indicating Müller gliosis, (C) RPE, and (D) fibroblasts.

(E and F) Examples of pseudo-bulk expression per cell type per donor are in (E) Müller and (F) RPE.

(G and H) RNAscope ISH for (G) *CRYAB* and (H) *CLU*. Representative images from macular sections of healthy controls (top panels) and GA (middle and bottom panels) from 3 donors each. Nearby sections were stained in (G) and (H), and the images were chosen for close vicinity in each donor. GA images are from the lesion, with lesion centers oriented to the right and the borders to the left. Dashed lines indicate removal of extra white space between the RPE and neural retina that was caused by artifactual postmortem retinal detachment.

See also Figure S3.

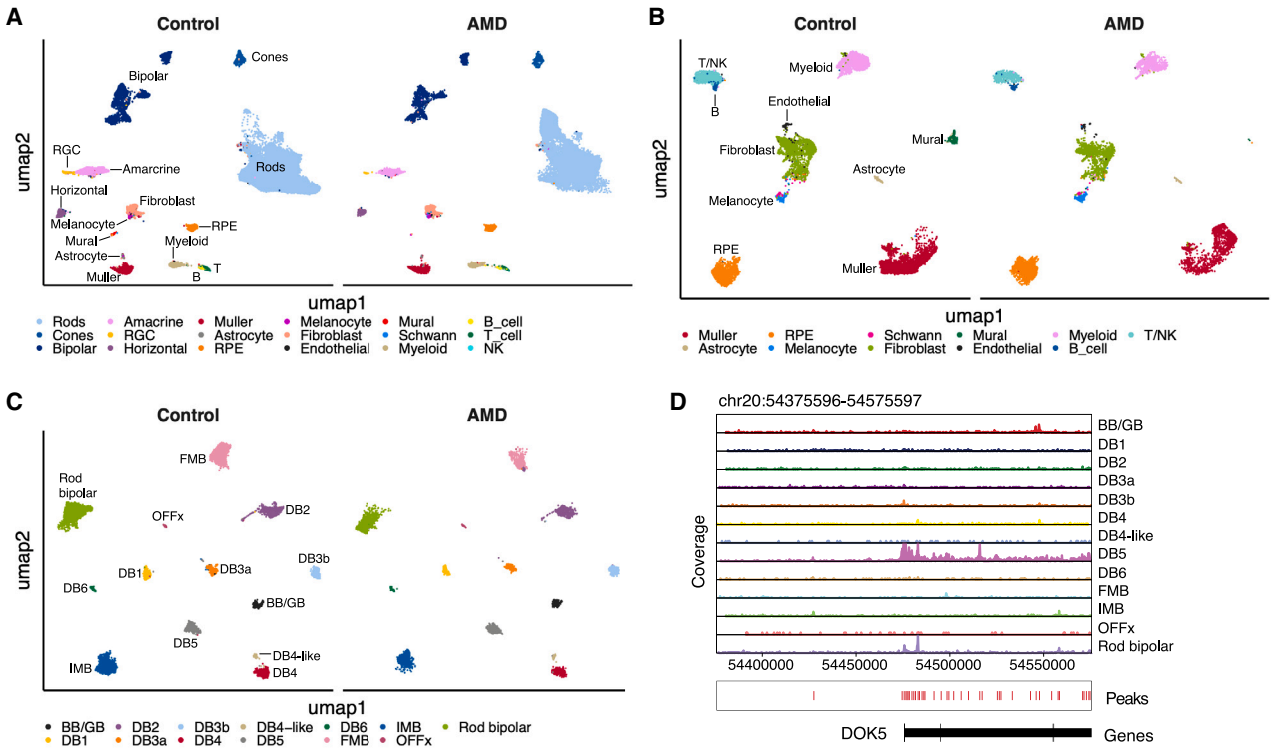

(legend on next page)

macular RPE/choroid (Figure 1B), further supports *HTRA1* as the causal gene in this locus. Similarly, the GWAS association upstream of *TNFRSF10A* overlaps a peak accessible in endothelial, myeloid, natural killer (NK), B, and T cells. Accessibility at this locus was correlated with expression of the nearby gene *TNFRSF10A* (Figure S4K; Table 2), suggesting this as a putative causal gene for AMD. In addition, chromatin accessibility at this GWAS locus was correlated with expression of adjacent family members, *TNFRSF10D* and *TNFRSF10B*, suggesting the presence of a *cis*-regulatory element (CRE) for multiple genes at this locus.

The top hit from the peak-to-gene analysis was *C6orf223/LINC03040* (Table 2; $R = 0.92$). The AMD GWAS SNP overlapping this peak was previously assigned to the nearby *VEGFA* locus. Intriguingly, a GWAS study in East Asians[33] found an independent association with risk of wet AMD at *C6orf223*, whereas no signal was detected for the *VEGFA* SNP in that population. This chromatin region was accessible in RPE and glial cells (Figure S5A), and *C6orf223* is an RPE-specific gene (Figure S5B), with enriched expression in the macula in our bulk RNA-seq dataset and in the foveal RPE (Figures S5C and S5D) in the Cowan et al.[18] single-cell RNA-seq (scRNA-seq) dataset. We did not detect the annotated small open reading frame in human RPE/choroid RNA by RT-PCR (data not shown). Instead, the RNA-seq pileup tracks in bulk ocular tissues were consistent with the Ensembl Canonical large intergenic non-coding RNA (lincRNA) transcript (ENST00000336600.6), which shares high homology only with other primates (Figure S5E). Taken together, our results suggest *C6orf223* may contribute to AMD risk in this GWAS locus, independent of and in addition to *VEGFA*, likely as a lincRNA with specialized function in the primate foveal RPE.

Single-nucleus profiling identifies cell types contributing to differential expression in AMD

We demonstrated the utility of our datasets for investigating cell type-specific expression in disease using the tyrosine kinase receptor KIT, an AMD-related gene detectable with high confidence by immunohistochemistry. *KIT* mRNA expression was significantly higher in dry AMD in bulk macular RPE/choroid and was higher in the periphery compared with the macula (Figure 5A). In the sNuc-seq, *KIT* showed specific expression in mast cells and melanocytes (Figure 5B) and in DB1 and OFFx bipolar cells of the retina (Figure S5F). In the snATAC-seq data, *KIT* showed open chromatin in melanocytes, RPE (Figure 5C), and two subtypes of bipolar cells (Figure S5G). Of the small number of melanocytes captured in the sNuc-seq, a higher percentage of KIT+ nuclei were from AMD (35%, 23/65) relative to control donors (15%, 16/105). In other cell types, the percentages of KIT+ nuclei were comparable between control and AMD.

To validate the specificity of *KIT* expression, we performed immunohistochemistry for CD117 (c-KIT) on macular sections from control, eAMD/iAMD, and GA. Across all disease states, a subset of neurons with bipolar cell morphology in the INL were positive for CD117 (Figures 5D and S5H), consistent with our sNuc-seq findings. In normal sections, CD117 protein was higher in peripheral than macular RPE, consistent with bulk RPE/choroid RNA-seq results (Figure 5A). In the choroid, the majority of CD117+ cells showed melanocyte characteristics of pigmentation and spindle morphology, and there were rarer unpigmented round CD117+ cells that we interpreted as mast cells (Figure 5D). In summary, we confirmed *KIT* expression in mast cells, bipolar cells, and melanocytes by immunohistochemistry, with melanocytes likely contributing to the differential expression between disease and control in macular bulk RNA-seq. Melanocytes comprise the majority of the choroidal cell population and share many molecular markers with RPE, including putative causal genes for AMD such as *TRPM1* and *TSPAN10*.[10] Further molecular characterization of choroidal melanocytes is needed to elucidate their role in AMD pathogenesis.

Expression profiles for genes associated with differentially methylated cytosines

We used our bulk RNA-seq and single-cell data to explore potential connections between methylation levels and gene expression. As described above, we annotated 35 genes to 23 differentially methylated CpGs in macular RPE/choroid (Figure 1E). Two of the 35 genes, *FRZB* and *TLE2*, were DE in control vs. GA (Figures 1H, 5E, and 5F), and both are WNT signaling regulators. The WNT antagonist *FRZB* was significantly increased in AMD macular RPE/choroid (Figure 5E) and was highly enriched in RPE and Müller glia (Figure 5G). Two DMPs are annotated to *TLE2* and *AES* (*TLE5*), which encode transcriptional co-repressors of WNT target genes. *TLE2* was highly expressed in fibroblasts and mural cells, followed by the RPE (Figure 5G), and showed reduced expression in diseased macula RPE/choroid (Figure 5F), whereas *AES* was not a DEG.

To better understand the role of differential methylation in these loci, we again performed peak-to-gene analysis, i.e., correlation between gene expression and chromatin accessibility in peaks overlapping DMPs. We found 32 genes with peak-to-gene expression correlation for 10 of the DMPs ($R > 0.3$; Table S1, ST1J), suggesting a regulatory relationship between the DMP

Figure 4. Single-nucleus ATAC sequencing of control and AMD donor eyes

(A–C) UMAP dimensionality reductions of chromatin accessibility in (A) major cell types, (B) non-neuronal cell types, and (C) bipolar cell subtypes.

(D) Genome tracks showing chromatin accessibility for *DOK5,* a marker gene for bipolar subtype DB5. x axis: the genomic position; y axis: normalized sequencing counts.

(E and F) UMAP of major cell types, colored by (E) ATAC accessibility of marker genes, or (F) expression of marker genes based on integration of sNuc-seq and single-nucleotide ATAC sequencing (snATAC-seq).

(G) Relationship of ocular cell types to genetic risk of AMD. UMAP of chromatin accessibility for major cell types, colored by the SCAVENGE trait relevance score.

(H) Genome tracks showing accessibility at the ARMS2-HTRA1 locus. The triangle marks the position of the peak overlapping the lead SNP rs3750846. Correlations between peaks and gene expression are shown as arcs connecting the peak and the transcription start site of *HTRA1,* and the arc color denotes the Pearson correlation *R*.

See also Figure S4.

Table 2. Linking gene expression to ATAC peaks overlapping GWAS loci for risk of AMD

GWAS locus name	Peak to gene	Correlation	FDR	GWAS SNP	GWAS chr	GWAS SNP (bp)	Peak start (bp)	Peak end (bp)	GWAS source
ARMS2/HTRA1	*HTRA1*	0.34	3.47E−14	rs3750846	chr10	122,456,049	122455943	122456443	AMD consortium: https://doi.org/10.1038/ng.3448
BLOC1S1/CD63/RHD5	*RDH5*	0.41	3.41E−21	rs3138141	chr12	55,721,994	55,721,543	55,722,043	AMD consortium: https://doi.org/10.1038/ng.3448
CNN2	*ARHGAP45*	0.46	3.96E−26	rs67538026	chr19	1,031,439	1,031,146	1,031,646	AMD consortium: https://doi.org/10.1038/ng.3448
	ABCA7	0.44	3.68E−24	rs67538026	chr19	1,031,439	1,031,146	1,031,646	
	TMEM259	0.3	4.55E−11	rs67538026	chr19	1,031,439	1,031,146	1,031,646	
	C19orf24	−0.32	2.81E−12	rs67538026	chr19	1,031,439	1,031,146	1,031,646	
	AZU1	−0.33	4.80E−13	rs67538026	chr19	1,031,439	1,031,146	1,031,646	
	MIDN	−0.34	3.84E−14	rs67538026	chr19	1,031,439	1,031,146	1,031,646	
	CBARP	−0.38	6.93E−18	rs67538026	chr19	1,031,439	1,031,146	1,031,646	
	GPX4	−0.45	6.20E−25	rs67538026	chr19	1,031,439	1,031,146	1,031,646	
NOTCH4	*AGPAT1*	0.43	1.16E−22	rs2071277	chr6	32,203,906	32,203,429	322,03,929	https://doi.org/10.1093/hmg/dds225
	CYP21A2	0.39	1.15E−18	rs2071277	chr6	32,203,906	32,203,429	322,03,929	
	HCG23	0.33	2.55E−13	rs2071277	chr6	32,203,906	32,203,429	32,203,929	
	RNF5	0.31	4.17E−12	rs2071277	chr6	32,203,906	32,203,429	32,203,929	
	PBX2	0.31	4.58E−12	rs2071277	chr6	32,203,906	32,203,429	32,203,929	
	TNXB	0.3	7.30E−11	rs2071277	chr6	32,203,906	32,203,429	32,203,929	
TNFRSF10A	*TNFRSF10A*	0.91	2.48E−187	rs79037040	chr8	23,225,458	23,225,044	23,225,544	AMD consortium: https://doi.org/10.1038/ng.3448
	TNFRSF10D	0.78	3.15E−100	rs79037040	chr8	23,225,458	23,225,044	23,225,544	
	TNFRSF10B	0.44	8.67E−24	rs79037040	chr8	23,225,458	23,225,044	23,225,544	
	LOXL2	−0.3	5.56E−11	rs79037040	chr8	23,225,458	23,225,044	23,225,544	
TRPM1	*TRPM1*	0.41	5.67E−21	rs7182946	chr15	31,102,665	31,102,411	31,102,911	https://doi.org/10.1167/iovs.17-21734
	MTMR10	0.4	1.31E−19	rs7182946	chr15	31,102,665	31,102,411	31,102,911	
	KLF13	−0.36	4.23E−16	rs6493454	chr15	31,101,742	31,101,260	31,101,760	
VEGFA	*C6orf223*	0.92	1.34E−202	rs943080	chr6	43,858,890	43,858,513	43,859,013	AMD consortium: https://doi.org/10.1038/ng.3448
	MRPS18A	0.77	1.91E−96	rs943080	chr6	43,858,890	43,858,513	43,859,013	
	VEGFA	0.47	5.45E−28	rs943080	chr6	43,858,890	43,858,513	43,859,013	

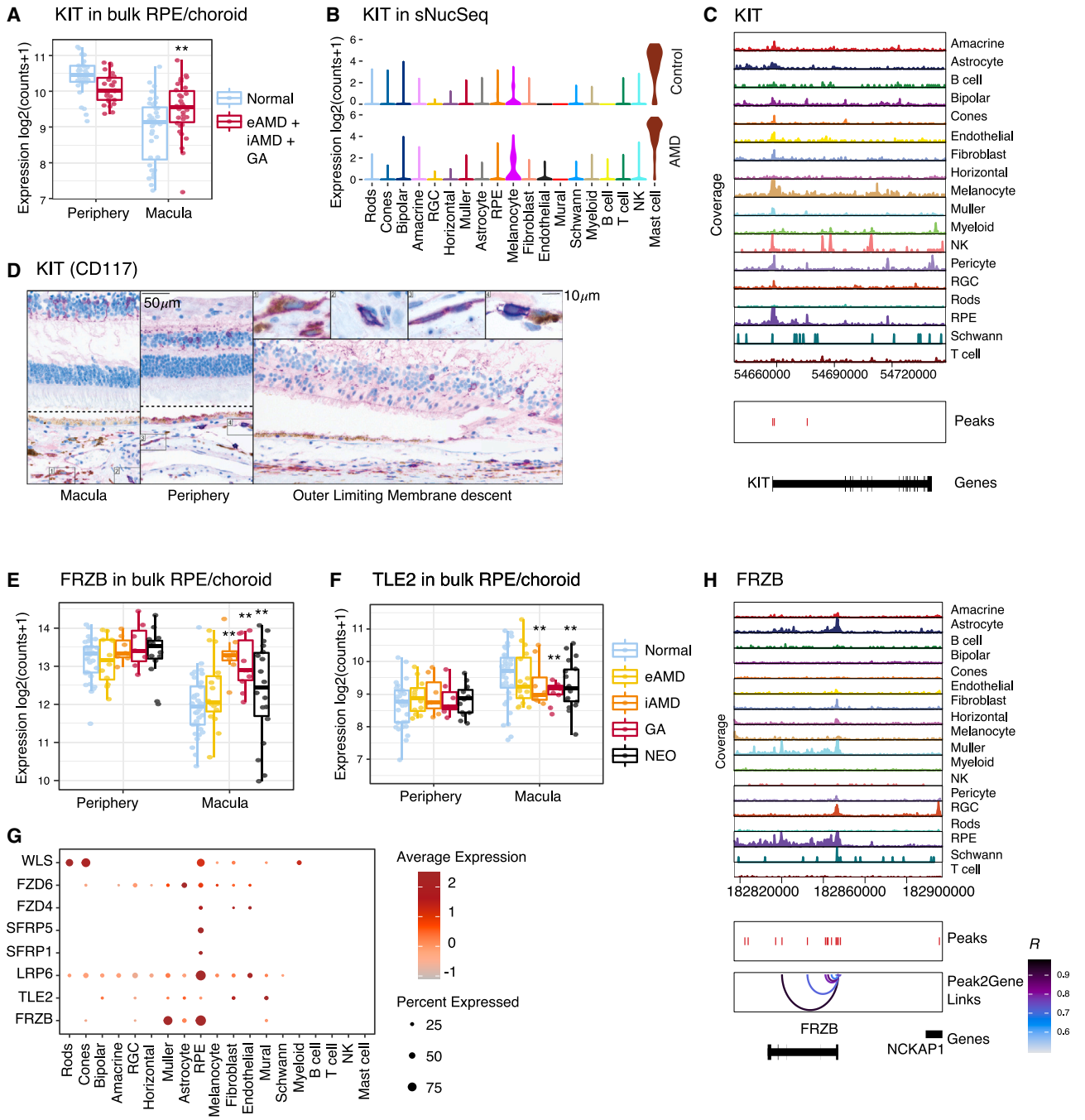

Figure 5. Integration of ocular data in AMD

(A) Normalized *KIT* gene expression in bulk RNA-seq from RPE/choroid. **FDR < 0.05 and fold change > 1.5. Boxplot is drawn from 25th to 75th percentiles, horizontal bars are medians, and whiskers show ranges.

(B) Violin plot showing normalized *KIT* expression across major cell types in sNuc-seq.

(C) Genome tracks showing accessibility of *KIT*.

(D) Immunohistochemistry staining for c-KIT/CD117. Representative images from control macula (left panel and insets 1 and 2), periphery (middle panel and insets 3 and 4), and macular sections of GA lesion borders (right panel). Choroidal melanocytes are CD117+ pigmented cells (insets 1 and 3), and mast cells are CD117+ cells with no pigmentation (insets 2 and 4). Dashed lines indicate removal of extra white space between the RPE and neural retina that was caused by artifactual postmortem retinal detachment.

(legend continued on next page)

loci and these genes. Indeed, the expression of 65% of these genes (21/32) was modulated in at least one of the AMD groups (FDR < 5%), with 4 genes DE in GA with FDR <5% and fold change >1.5 (*FRZB*, *TLE2*, *CD52*, and *MAN2C1*). *FRZB* showed the highest correlation between expression and chromatin accessibility at the DMP/CpG island (Figure 5H; $R = 0.86$). These results indicate that a regulatory element in this locus may underlie transcriptional changes in *FRZB* in the context of dry AMD. Evidence for a regulatory element is supported by ENCODE prediction of a CRE in the same region,[44,45] and a *cis*-protein quantitative trait locus (pQTL) mapping to that locus in the plasma.[46,47] Taken together, our results suggest a correlation among CpG methylation, chromatin accessibility, and gene expression in these loci and illustrate the utility of an integrative approach to understand loci in non-coding regions beyond the nearest genes. The complete list of genes annotated to DMPs and the differential expression results for these genes are in Table S1 (ST1B and ST1J).

WNT signaling pathway in dry AMD

Three genes annotated to methylation DMPs (*TLE2*, *AES*, and *FRZB*) are negative regulators of the canonical WNT signaling pathway. The DMPs in *TLE2* and *FRZB* showed a correlation between accessibility and gene expression ($R > 0.3$), and both genes are DE in AMD in bulk RNA-seq (FDR < 5% and fold change > 1.5). The observations from disease tissues alone, however, are insufficient to indicate a causal role of the pathway in disease. To interrogate the contribution of these WNT regulatory genes to genetic risk of GA/dry AMD, we performed a rare variant burden test[48] for these 3 WNT pathway genes comparing 1,707 GA cases with 2,611 non-AMD controls (STAR Methods; Table S1, ST1A). Of the three, rare variant burden was associated with risk of GA only in *TLE2* (odds ratio [OR] = 2.64; adjusted p = 0.009), where rare variants are predicted to result in reduced activity of *TLE2*, suggesting a causal role for the WNT pathway in the risk of dry AMD.

To further characterize the canonical WNT pathway in AMD, we examined DE expression in the core WNT components and modulators (Table S1, ST1K). In bulk RPE/choroid RNA-seq, we found 24 WNT core canonical genes DE in AMD groups (FDR < 5%), and 10 of these genes showed a fold change >1.5 (*APC*, *DKK2*, *FRZB*, *FZD10*, *NKD2*, *RSPO4*, *SOST*, *SOSTDC1*, *TLE2*, *WNT9A*). In the WNT core PCP pathway, we found 14 genes DE in AMD groups (FDR < 5%), and 2 of these (*DAAM1*, *WNT11*) showed a fold change >1.5. In our sNuc-seq, WNT pathway genes showed specific enrichment in RPE cells, including *SFRP1* and *SFRP5*, closely related to *FRZB*/*SFRP3* (Figure 5G). Taken together, multiple lines of evidence from our disease data point to the dysregulation of WNT signaling in RPE cells as a feature of dry AMD.

DISCUSSION

Deciphering mechanisms driving AMD onset and progression has been a major challenge. The diversity of risk factors and their interactions, the heterogeneous disease presentation and progression, and the lack of appropriate *in vivo* and *in vitro* models are obstacles to translational research in multifactorial ophthalmic diseases. For AMD, the nature of the disease and the inaccessibility of the affected tissues compounds these barriers to molecular characterization. The macula is a uniquely primate, intricate structure <6 mm in diameter. AMD phenotypes such as drusen and GA lesions are confined to this region and are only found in humans. To date, animal models do not recapitulate the full spectrum of phenotypes observed in the human condition. Furthermore, the patchiness of AMD lesions results in spatial variability of cellular dysfunction within the macula. Last but not least, the retina and RPE/choroid quickly undergo degradation postmortem, posing a logistical challenge for human sample banking.

To overcome these obstacles, here we used a multifaceted approach to investigate the epigenetic and transcriptional mechanisms underlying AMD. To address the issue of disease heterogeneity, tissues used for bulk analyses were carefully chosen from a collection of phenotyped human ocular tissue, where the controls showed little or no signs of drusen, and the disease tissues were delineated by clinical staging criteria. This is important, as we observed that at least 30% of presumed "normal" donors >60 years of age showed disease pathophysiology.[2] Lack of well-characterized phenotypes can introduce artifacts in downstream molecular experiments. The attention to postmortem interval (PMI) time, in tandem with rigorous phenotyping and dissecting procedures, is critical for data quality. As we and others have demonstrated, transcriptomic and epigenetic changes can be a reflection of long PMI rather than of underlying disease mechanisms.[2,49]

To better understand the cellular complexity in AMD eyes, we employed single-cell genomics to complement and validate our bulk-tissue approach; our single-cell approach provides cell type information, and our bulk tissue provides a more complete molecular landscape. While many single-cell genomics studies of the human eye are publicly available, these datasets are primarily sampling the retinal cells with little or no representation of RPE cells. Furthermore, the vast majority of the donor eyes in the published studies are without disease diagnosis.[18,24,26,27,29] To date, the most comprehensive single-cell study of AMD choroid tissue is from Voigt et al.,[27] which included 10 controls and 9 eAMD and 2 NEO donors. Their dataset contained large proportions of fibroblasts, endothelial cells, and pericytes but few RPE cells. Our integrative approach (1) addresses the scarce information from AMD RPE and retinal cell

(E and F) Normalized gene expression in bulk RNA-seq from RPE/choroid for (E) *FRZB* and (F) *TLE2*. **FDR < 0.05 and fold change > 1.5. Boxplots are drawn from 25th to 75th percentiles, horizontal bars are medians, and whiskers show ranges.
(G) Dotplot showing expression in sNuc-seq for WNT pathway genes enriched in RPE.
(H) Genome tracks showing accessibility of *FRZB*. Correlations between peaks and gene expression are shown as arcs connecting the peak and the transcription start site of *FRZB*. *R*, Pearson correlation coefficient.
See also Figure S5.

types in the public domain, (2) identifies cell type-specific transcriptomic shifts in retinal diseases, and (3) provides cell type-specific chromatin accessibility from control and AMD ocular tissues.

Our data bridge a major knowledge gap in AMD biology and enable the identification of novel molecular signatures associated with AMD. Importantly, while we found hundreds of DEGs in the macular RPE/choroid comparisons, none were DE in the periphery. This stark difference solidifies the need for regional dissection of ocular tissue. In addition to the DEGs in bulk tissues, we also identified genome-wide significant differences in DNA methylation between control and GA macular RPE/choroid. At every DMP, the methylation levels for eAMD/iAMD fell between control and GA groups, although there were no significant DMPs between control and eAMD/iAMD. This suggests that rigorous postmortem phenotyping and the focus on the macular tissue both improved the signal-to-noise ratio in our methylation analysis.

Our sNuc-seq analysis uncovered a prominent gene expression shift in Müller glia, which are specialized macroglia essential for retinal maintenance including fluid/ionic homeostasis, metabolic and neurotrophic support, redox regulation, and the cone visual cycle.[50] In disease and injury conditions, Müller glia exhibit a gliotic phenotype characterized by *GFAP* upregulation.[51–54] Our results indicate that Müller gliosis is not a general feature of AMD, consistent with studies of bulk RNA-seq in AMD retina.[10,30] This observation highlights the molecular discrepancy between retinal injury models often used in AMD translational research and the actual human disease state,[54] which may be misleading. The gliotic state appears to be a crucial intermediate between normal Müller glia and the stem cell identity in retinal regeneration.[55–59] As retinal regeneration gains momentum as a therapeutic strategy, it is important to establish a deeper understanding of disease Müller glia, as these are top contenders for endogenous stem cells, and potential therapeutics designed to reprogram the basal or gliotic Müller may not be suitable for the AMD-like state.

We found higher expression of the drusen components clusterin/*CLU*[60,61] and *CRYAB* in AMD Müller glia. Clusterin is a known substrate of the protease HTRA1,[62,63] a top candidate gene associated with AMD incidence and progression.[6,64] *CRYAB* is a widely expressed small heat shock protein enriched in AMD soft drusen.[60] In mouse models of retinal neovascularization, the absence of *CRYAB* reduced VEGFA protein levels and vascular phenotypes.[65] *CRYAB* is also involved in inflammatory responses in multiple neurodegenerative diseases[66–71] and is generally described as neuroprotective.[72,73] In the human eye, *CRYAB* has been found in epiretinal membranes in proliferative diabetic retinopathy.[74] We found elevated *CRYAB* and *CLU* in GA relative to controls but not in iAMD, suggesting these changes are more likely to be tissue responses to degeneration rather than the cause.

In our study, *FRZB* and *TLE2* emerged as WNT pathway genes of particular interest for dry AMD. Both are negative regulators of WNT signaling with multiple family members expressed in RPE. *FRZB* was previously identified as a putative substrate for the HTRA1 protease,[62] providing a potential link to the top locus for AMD risk and progression. Hypermethylation of *FRZB* in various cancers has been associated with reduced expression and worse outcomes.[75–79] Here, increased CpG methylation at *FRZB* correlated with higher expression in the AMD macular RPE/choroid. We found that DMPs in *FRZB* and *TLE2* occur in open chromatin regions (Figure 5H; Table S1, ST1J), where chromatin accessibility was correlated with gene expression, suggesting putative regulatory elements at these methylation loci. This hypothesis is supported by published results from ENCODE predicting a CRE in the *FRZB* DMP locus.[44,45]

In addition to *FRZB* and *TLE2*, we identified multiple core WNT pathway components that are DE in AMD, including the coreceptor *LRP6* and *APC*. However, postmortem analysis is a snapshot of pathophysiology, and caution must be taken in interpreting the direction of transcriptional changes, which could reflect either causal mechanisms or mitigating responses to ongoing degeneration. Our observation that rare variants in *TLE2* were associated with GA supports the hypothesis that weakened inhibition of WNT signaling may be driving increased risk for GA. Aberrant WNT activation has been linked to retinal vascular diseases such as diabetic retinopathy and wet AMD.[80] In RPE cell culture, WNT/β-catenin signaling promotes loss of epithelial morphology, cell cycle reentry, and cell migration.[81–84] Notably, *CRYAB* is also known to promote loss of epithelial features in RPE,[85] suggesting that the *CRYAB* upregulation we observed in GA lesions could participate in the same cellular processes as WNT activation.

The ARMS2/HTRA1 and the complement loci are of particular interest given the strong human genetics evidence across multiple studies of AMD risk and progression. Among the complement genes, we found that *CFI* was elevated in macular RPE/choroid in dry AMD (FDR < 5%; Table S1, ST1B). In the eye, *CFH* is highly expressed in the RPE/choroid compared with the retina,[10,26,27,86] with enriched expression in choroidal fibroblasts and RPE. Here, we did not find DE, differential methylation, or chromatin accessibility peak-to-gene correlations for *CFH*. However, recent allele-specific expression data suggest that *CFH* expression in the RPE/choroid may be modulated by genetic variants associated with risk of AMD (unpublished data).

The disease mechanisms underlying the ARMS2/HTRA1 GWAS locus are still unclear. *ARMS2* expression levels are very low across ocular and extraocular tissues, and *HTRA1* encodes an extracellular protease with various ocular substrates.[62,63] Functional studies suggest that *HTRA1* variants may alter codon usage and expression.[87,88] In the eye, *HTRA1* is expressed in many cell types, with the strongest immunohistochemistry (IHC) signals in the INL and the Bruch's membrane,[62,89] consistent with expression in horizontal cells and RPE. Early semi-quantitative studies with small sample sizes[90,91] suggested that the risk allele was associated with higher *HTRA1* expression, whereas a recent large study of primarily control tissues showed the opposite effect in RPE.[89] Comparisons between disease and control retina have consistently shown no difference in multiple studies,[10,25,92] but RPE/choroid data are scarce, with mixed results.[89,90,93] We previously identified *HTRA1* as the putative causal gene in the ARMS2/HTRA1 locus based on co-localization between the AMD GWAS signal and ocular expression QTL (eQTL).[10] Here, our results showed a disease-related increase in *HTRA1* expression in the macular tissue

and pointed to a regulatory element at the GWAS locus driving *HTRA1* (Figure 4H). While it is still unclear whether *HTRA1* expression is associated with increased risk or protection in AMD, our findings further strengthen the case for *HTRA1* as a causal gene for AMD.

Our comprehensive molecular analysis is a major step toward understanding AMD pathogenesis and yielded a wealth of genes with relevance to disease mechanisms in human AMD. With recent advances in patient-derived induced pluripotent stem cells, CRISPR gene editing technologies, and the expanding toolbox of *in vitro* RPE maturation and stress models, the AMD field has an unprecedented opportunity to dissect the disease mechanisms. Given the limitations of *in vitro* and *in vivo* models, especially in the context of modeling aging tissue, it is critical to benchmark these findings against high-quality data from normal and disease human tissues. The information presented here will be vital for developing hypotheses, for linking *in vitro* and *in vivo* models to human disease, and for providing greater precision in our therapeutic approach to AMD treatment and prevention.

Limitations of the study

Limitations of bulk-tissue analyses include a lack of cell type and spatial resolution. We performed single-cell analyses to achieve cell type resolution, but future studies using high-resolution spatial transcriptomics in RPE are needed to address the latter.

Limitations of differential expression analyses include (1) changes may be secondary and not causal, and (2) change in expression does not imply direction of effect in disease. Integration with genetics and perturbation studies in model systems are needed to elucidate the effects of expression changes on disease.

sNuc-seq enables comparison of transcriptomics across frozen tissues, but since the cytosolic transcripts are lost during lysis, the data obtained are nuclear specific and more sparse than single cell.

Shared limitations for both the sNuc-seq and snATAC-seq data include (1) the number of donors is relatively small, (2) the donor eyes were not phenotyped, and the macula was not separated from the periphery, and (3) the protocols were optimized for retina/RPE but not for choroidal cells. Future studies with larger collections of phenotyped and dissected tissues using tissue-specific protocols would overcome these limitations.

The progression risk gene *TLE2* reported here was significant among the 3 genes tested and did not reach genome-wide significance. Additional replication cohorts are needed to increase the confidence of this observation.

STAR★METHODS

Detailed methods are provided in the online version of this paper and include the following:

- KEY RESOURCES TABLE
- RESOURCE AVAILABILITY
  - Lead contact
  - Materials availability
  - Data and code availability
- EXPERIMENTAL MODEL AND SUBJECT DETAILS
- METHOD DETAILS
  - Human donor eyes for bulk tissue analysis
  - Bulk RNAseq
  - DNA methylation microarray
  - Human donor eyes for single-cell analyses and *in situ* hybridization
  - Single-nucleus RNAseq (sNucSeq)
  - Single-nucleus ATACseq (snATAC-seq)
  - Immunohistochemistry and RNAscope *in situ* hybridization
- QUANTIFICATION AND STATISTICAL ANALYSIS
  - Number of samples
  - RNAseq in bulk RPE/choroid RNAseq from phenotyped donors
  - DNA methylation in bulk RPE/choroid RNAseq from phenotyped donors
  - Single-nucleus RNAseq (sNucSeq) analysis
  - Single-nucleus ATAC-seq (snATAC-seq)
  - Single-cell enrichments for AMD GWAS loci
  - Rare variant burden test
  - Phylogenetic tree

SUPPLEMENTAL INFORMATION

Supplemental information can be found online at https://doi.org/10.1016/j.xgen.2023.100302.

ACKNOWLEDGMENTS

We thank the patients and their families who contributed samples to this study; the Lion's Eye Institute for procuring human eyes; the Next Generation Sequencing team (Genentech) and the Human Tissue Lab (Genentech) for sample processing and managing; Jason Vander Heiden and Brad Friedman for cell-type-specific gene signatures; Zora Modrusan, Alicia Nugent, Shawntay Chaney, Katie Litts, and Simon Gao for helpful discussions; and Allison K. Bruce for creating the graphical abstract. This work was funded by Genentech/Roche, The Macular Degeneration Foundation, Inc. (Henderson, NV, USA; M.M.D.), The Carl Marshall Reeves & Mildred Almen Reeves Foundation, Inc. (Fenton, MO, USA; M.M.D.), NIH grants 1K08EY031800-01 and EY0114800, and an unrestricted grant from Research to Prevent Blindness (New York, NY, USA) to the Department of Ophthalmology & Visual Sciences, University of Utah. J.H.L. is supported by NIH/NCATS grant UL1TR0012-05.

AUTHOR CONTRIBUTIONS

Conceptualization, H.-H.C., L.D.O., and M.M.D.; methodology, H.-H.C., L.D.O., M.M.D., L.A.O., and L.A.F.; investigation, L.A.O., I.K.K., A. Shakoor, J.H.L., C.Z., H.-H.C., J.L., J.H., J.T., S.H., A. Sridhar, M.H.F., E.A., N.H., J.L.B., R.F., R.A.Z., E.C.G., R.S., L.A.F., and M.M.D.; software, L.D.O., V.T.M., and C.C.; formal analysis, L.D.O., V.T.M., C.C., O.M., A.D.S., and B.L.Y.; data curation, R.S.; visualization, L.D.O. and V.T.M.; writing, H.-H.C., L.D.O., L.A.O., and M.M.D.; resources, J.S.K.; project administration, M.J.T., H.-H.C., and M.M.D.; funding acquisition, M.J.T., J.S.K., and M.M.D.

DECLARATION OF INTERESTS

L.D.O., J.H., A.D.S., J.T., S.H., V.T.M., C.C., J.L., A. Sridhar, O.M., J.S.K., M.J.T., B.L.Y., and H.-H.C. are employees and shareholders of Genentech/Roche. I.K.K. is a consultant for Kodiak Sciences and Biophytis and receives research funding from Allergen. M.M.D. has a research grant from Genentech/Roche.

INCLUSION AND DIVERSITY

One or more of the authors of this paper self-identifies as an underrepresented ethnic minority in their field of research or within their geographical location. One or more of the authors of this paper self-identifies as a gender minority in their field of research. We support inclusive, diverse, and equitable conduct of research.

Received: October 3, 2022
Revised: January 21, 2023
Accepted: March 22, 2023
Published: April 18, 2023

REFERENCES

1. Wong, W.L., Su, X., Li, X., Cheung, C.M.G., Klein, R., Cheng, C.-Y., and Wong, T.Y. (2014). Global prevalence of age-related macular degeneration and disease burden projection for 2020 and 2040: a systematic review and meta-analysis. Lancet. Glob. Health *2*, e106–e116.
2. Owen, L.A., Shakoor, A., Morgan, D.J., Hejazi, A.A., McEntire, M.W., Brown, J.J., Farrer, L.A., Kim, I., Vitale, A., and DeAngelis, M.M. (2019). The Utah protocol for postmortem eye phenotyping and molecular biochemical analysis. Invest. Ophthalmol. Vis. Sci. *60*, 1204–1212.
3. Age-Related Eye Disease Study Research Group (2001). A randomized, placebo-controlled, clinical trial of high-dose supplementation with vitamins C and E, beta carotene, and zinc for age-related macular degeneration and vision loss: AREDS report no. 8. Arch. Ophthalmol. *119*, 1417–1436.
4. Evans, J.R., and Lawrenson, J.G. (2017). Antioxidant vitamin and mineral supplements for slowing the progression of age-related macular degeneration. Cochrane Database Syst. Rev. *7*, CD000254.
5. Pennington, K.L., and DeAngelis, M.M. (2016). Epidemiology of age-related macular degeneration (AMD): associations with cardiovascular disease phenotypes and lipid factors. Eye Vis. *3*, 34.
6. Fritsche, L.G., Igl, W., Bailey, J.N.C., Grassmann, F., Sengupta, S., Bragg-Gresham, J.L., Burdon, K.P., Hebbring, S.J., Wen, C., Gorski, M., et al. (2016). A large genome-wide association study of age-related macular degeneration highlights contributions of rare and common variants. Nat. Genet. *48*, 134–143.
7. Fritsche, L.G., Chen, W., Schu, M., Yaspan, B.L., Yu, Y., Thorleifsson, G., Zack, D.J., Arakawa, S., Cipriani, V., Ripke, S., et al. (2013). Seven new loci associated with age-related macular degeneration. Nat. Genet. *45*, 433–439. 439e1-2.
8. Zhang, C., Owen, L.A., Lillvis, J.H., Zhang, S.X., Kim, I.K., and DeAngelis, M.M. (2022). AMD genomics: non-coding RNAs as biomarkers and therapeutic targets. J. Clin. Med. *11*, 1484. https://doi.org/10.3390/jcm11061484.
9. DeAngelis, M.M., Owen, L.A., Morrison, M.A., Morgan, D.J., Li, M., Shakoor, A., Vitale, A., Iyengar, S., Stambolian, D., Kim, I.K., et al. (2017). Genetics of age-related macular degeneration (AMD). Hum. Mol. Genet. *26*, R45–R50.
10. Orozco, L.D., Chen, H.-H., Cox, C., Katschke, K.J., Jr., Arceo, R., Espiritu, C., Caplazi, P., Nghiem, S.S., Chen, Y.-J., Modrusan, Z., et al. (2020). Integration of eQTL and a single-cell atlas in the human eye identifies causal genes for age-related macular degeneration. Cell Rep. *30*, 1246–1259.e6.
11. Seddon, J.M., McLeod, D.S., Bhutto, I.A., Villalonga, M.B., Silver, R.E., Wenick, A.S., Edwards, M.M., and Lutty, G.A. (2016). Histopathological insights into choroidal vascular loss in clinically documented cases of age-related macular degeneration. JAMA Ophthalmol. *134*, 1272–1280.
12. Mandai, M., Watanabe, A., Kurimoto, Y., Hirami, Y., Morinaga, C., Daimon, T., Fujihara, M., Akimaru, H., Sakai, N., Shibata, Y., et al. (2017). Autologous induced stem-cell-derived retinal cells for macular degeneration. N. Engl. J. Med. *376*, 1038–1046.
13. Sharma, R., Khristov, V., Rising, A., Jha, B.S., Dejene, R., Hotaling, N., Li, Y., Stoddard, J., Stankewicz, C., Wan, Q., et al. (2019). Clinical-grade stem cell-derived retinal pigment epithelium patch rescues retinal degeneration in rodents and pigs. Sci. Transl. Med. *11*, eaat5580. https://doi.org/10.1126/scitranslmed.aat5580.
14. Sharma, R., George, A., Nimmagadda, M., Ortolan, D., Karla, B.-S., Qureshy, Z., Bose, D., Dejene, R., Liang, G., Wan, Q., et al. (2021). Epithelial phenotype restoring drugs suppress macular degeneration phenotypes in an iPSC model. Nat. Commun. *12*, 7293.
15. Handa, J.T., Bowes Rickman, C., Dick, A.D., Gorin, M.B., Miller, J.W., Toth, C.A., Ueffing, M., Zarbin, M., and Farrer, L.A. (2019). A systems biology approach towards understanding and treating non-neovascular age-related macular degeneration. Nat. Commun. *10*, 3347.
16. Deangelis, M.M., Silveira, A.C., Carr, E.A., and Kim, I.K. (2011). Genetics of age-related macular degeneration: current concepts, future directions. Semin. Ophthalmol. *26*, 77–93.
17. Peng, Y.-R., Shekhar, K., Yan, W., Herrmann, D., Sappington, A., Bryman, G.S., van Zyl, T., Do, M.T.H., Regev, A., and Sanes, J.R. (2019). Molecular classification and comparative taxonomics of foveal and peripheral cells in primate retina. Cell *176*, 1222–1237.e22.
18. Cowan, C.S., Renner, M., De Gennaro, M., Gross-Scherf, B., Goldblum, D., Hou, Y., Munz, M., Rodrigues, T.M., Krol, J., Szikra, T., et al. (2020). Cell types of the human retina and its organoids at single-cell resolution. Cell *182*, 1623–1640.e34.
19. Finkbeiner, C., Ortuño-Lizarán, I., Sridhar, A., Hooper, M., Petter, S., and Reh, T.A. (2022). Single-cell ATAC-seq of fetal human retina and stem-cell-derived retinal organoids shows changing chromatin landscapes during cell fate acquisition. Cell Rep. *38*, 110294.
20. Senabouth, A., Daniszewski, M., Lidgerwood, G.E., Liang, H.H., Hernández, D., Mirzaei, M., Keenan, S.N., Zhang, R., Han, X., Neavin, D., et al. (2022). Transcriptomic and proteomic retinal pigment epithelium signatures of age-related macular degeneration. Nat. Commun. *13*, 4233.
21. Menon, M., Mohammadi, S., Davila-Velderrain, J., Goods, B.A., Cadwell, T.D., Xing, Y., Stemmer-Rachamimov, A., Shalek, A.K., Love, J.C., Kellis, M., et al. (2019). Single-cell transcriptomic atlas of the human retina identifies cell types associated with age-related macular degeneration. Nat. Commun. *10*, 4902.
22. Lyu, Y., Zauhar, R., Dana, N., Strang, C.E., Hu, J., Wang, K., Liu, S., Pan, N., Gamlin, P., Kimble, J.A., et al. (2021). Implication of specific retinal cell-type involvement and gene expression changes in AMD progression using integrative analysis of single-cell and bulk RNA-seq profiling. Sci. Rep. *11*, 15612.
23. Zauhar, R., Biber, J., Jabri, Y., Kim, M., Hu, J., Kaplan, L., Pfaller, A.M., Schäfer, N., Enzmann, V., Schlötzer-Schrehardt, U., et al. (2022). As in real estate, location matters: cellular expression of complement varies between macular and peripheral regions of the retina and supporting tissues. Front. Immunol. *13*, 895519.
24. Wang, S.K., Nair, S., Li, R., Kraft, K., Pampari, A., Patel, A., Kang, J.B., Luong, C., Kundaje, A., and Chang, H.Y. (2022). Single-cell multiome of the human retina and deep learning nominate causal variants in complex eye diseases. Cell Genom. *2*, 100164.
25. Ratnapriya, R., Sosina, O.A., Starostik, M.R., Kwicklis, M., Kapphahn, R.J., Fritsche, L.G., Walton, A., Arvanitis, M., Gieser, L., Pietraszkiewicz, A., et al. (2019). Retinal transcriptome and eQTL analyses identify genes associated with age-related macular degeneration. Nat. Genet. *51*, 606–610.
26. Voigt, A.P., Mulfaul, K., Mullin, N.K., Flamme-Wiese, M.J., Giacalone, J.C., Stone, E.M., Tucker, B.A., Scheetz, T.E., and Mullins, R.F. (2019). Single-cell transcriptomics of the human retinal pigment epithelium and choroid in health and macular degeneration. Proc. Natl. Acad. Sci. USA *116*, 24100–24107.
27. Voigt, A.P., Mullin, N.K., Mulfaul, K., Lozano, L.P., Wiley, L.A., Flamme-Wiese, M.J., Boese, E.A., Han, I.C., Scheetz, T.E., Stone, E.M., et al. (2022). Choroidal endothelial and macrophage gene expression in

atrophic and neovascular macular degeneration. Hum. Mol. Genet. *31*, 2406–2423.

28. Holliday, E.G., Smith, A.V., Cornes, B.K., Buitendijk, G.H.S., Jensen, R.A., Sim, X., Aspelund, T., Aung, T., Baird, P.N., Boerwinkle, E., et al. (2013). Insights into the genetic architecture of early stage age-related macular degeneration: a genome-wide association study meta-analysis. PLoS One *8*, e53830.
29. Yan, W., Peng, Y.-R., van Zyl, T., Regev, A., Shekhar, K., Juric, D., and Sanes, J.R. (2020). Cell atlas of the human Fovea and peripheral retina. Sci. Rep. *10*, 9802.
30. Ratnapriya, R., Sosina, O.A., Starostik, M.R., Kwicklis, M., Kapphahn, R.J., Fritsche, L.G., Walton, A., Arvanitis, M., Gieser, L., Pietraszkiewicz, A., et al. (2019). Retinal transcriptome and eQTL analyses identify genes associated with age-related macular degeneration. Nat. Genet. *51*, 606–610. https://doi.org/10.1038/s41588-019-0351-9.
31. Cipriani, V., Leung, H.-T., Plagnol, V., Bunce, C., Khan, J.C., Shahid, H., Moore, A.T., Harding, S.P., Bishop, P.N., Hayward, C., et al. (2012). Genome-wide association study of age-related macular degeneration identifies associated variants in the TNXB-FKBPL-NOTCH4 region of chromosome 6p21.3. Hum. Mol. Genet. *21*, 4138–4150.
32. Persad, P.J., Heid, I.M., Weeks, D.E., Baird, P.N., de Jong, E.K., Haines, J.L., Pericak-Vance, M.A., and Scott, W.K.; International Age-Related Macular Degeneration Genomics Consortium IAMDGC (2017). Joint analysis of nuclear and mitochondrial variants in age-related macular degeneration identifies novel loci TRPM1 and ABHD2/RLBP1. Invest. Ophthalmol. Vis. Sci. *58*, 4027–4038.
33. Cheng, C.-Y., Yamashiro, K., Chen, L.J., Ahn, J., Huang, L., Huang, L., Cheung, C.M.G., Miyake, M., Cackett, P.D., Yeo, I.Y., et al. (2015). New loci and coding variants confer risk for age-related macular degeneration in East Asians. Nat. Commun. *6*, 6063.
34. Arakawa, S., Takahashi, A., Ashikawa, K., Hosono, N., Aoi, T., Yasuda, M., Oshima, Y., Yoshida, S., Enaida, H., Tsuchihashi, T., et al. (2011). Genome-wide association study identifies two susceptibility loci for exudative age-related macular degeneration in the Japanese population. Nat. Genet. *43*, 1001–1004.
35. Guindo-Martínez, M., Amela, R., Bonàs-Guarch, S., Puiggròs, M., Salvoro, C., Miguel-Escalada, I., Carey, C.E., Cole, J.B., Rüeger, S., Atkinson, E., et al. (2021). The impact of non-additive genetic associations on age-related complex diseases. Nat. Commun. *12*, 2436.
36. Yu, Y., Bhangale, T.R., Fagerness, J., Ripke, S., Thorleifsson, G., Tan, P.L., Souied, E.H., Richardson, A.J., Merriam, J.E., Buitendijk, G.H.S., et al. (2011). Common variants near FRK/COL10A1 and VEGFA are associated with advanced age-related macular degeneration. Hum. Mol. Genet. *20*, 3699–3709.
37. Yan, Q., Ding, Y., Liu, Y., Sun, T., Fritsche, L.G., Clemons, T., Ratnapriya, R., Klein, M.L., Cook, R.J., Liu, Y., et al. (2018). Genome-wide analysis of disease progression in age-related macular degeneration. Hum. Mol. Genet. *27*, 929–940.
38. Grunin, M., Beykin, G., Rahmani, E., Schweiger, R., Barel, G., Hagbi-Levi, S., Elbaz-Hayoun, S., Rinsky, B., Ganiel, M., Carmi, S., et al. (2020). Association of a variant in VWA3A with response to anti-vascular endothelial growth factor treatment in neovascular AMD. Invest. Ophthalmol. Vis. Sci. *61*, 48.
39. Winkler, T.W., Grassmann, F., Brandl, C., Kiel, C., Günther, F., Strunz, T., Weidner, L., Zimmermann, M.E., Korb, C.A., Poplawski, A., et al. (2020). Genome-wide association meta-analysis for early age-related macular degeneration highlights novel loci and insights for advanced disease. BMC Med. Genomics *13*, 120.
40. Wang, J., Zibetti, C., Shang, P., Sripathi, S.R., Zhang, P., Cano, M., Hoang, T., Xia, S., Ji, H., Merbs, S.L., et al. (2018). ATAC-Seq analysis reveals a widespread decrease of chromatin accessibility in age-related macular degeneration. Nat. Commun. *9*, 1364.
41. Yu, F., Cato, L.D., Weng, C., Liggett, L.A., Jeon, S., Xu, K., Chiang, C.W.K., Wiemels, J.L., Weissman, J.S., de Smith, A.J., et al. (2022). Variant to function mapping at single-cell resolution through network propagation. Nat. Biotechnol. *40*, 1644–1653.
42. Zhu, Z., Zhang, F., Hu, H., Bakshi, A., Robinson, M.R., Powell, J.E., Montgomery, G.W., Goddard, M.E., Wray, N.R., Visscher, P.M., et al. (2016). Integration of summary data from GWAS and eQTL studies predicts complex trait gene targets. Nat. Genet. *48*, 481–487.
43. Granja, J.M., Corces, M.R., Pierce, S.E., Bagdatli, S.T., Choudhry, H., Chang, H.Y., and Greenleaf, W.J. (2021). ArchR is a scalable software package for integrative single-cell chromatin accessibility analysis. Nat. Genet. *53*, 403–411.
44. ENCODE Project Consortium (2012). An integrated encyclopedia of DNA elements in the human genome. Nature *489*, 57–74.
45. Luo, Y., Hitz, B.C., Gabdank, I., Hilton, J.A., Kagda, M.S., Lam, B., Myers, Z., Sud, P., Jou, J., Lin, K., et al. (2020). New developments on the Encyclopedia of DNA Elements (ENCODE) data portal. Nucleic Acids Res. *48*, D882–D889.
46. Sun, B.B., Maranville, J.C., Peters, J.E., Stacey, D., Staley, J.R., Blackshaw, J., Burgess, S., Jiang, T., Paige, E., Surendran, P., et al. (2018). Genomic atlas of the human plasma proteome. Nature *558*, 73–79.
47. Gudjonsson, A., Gudmundsdottir, V., Axelsson, G.T., Gudmundsson, E.F., Jonsson, B.G., Launer, L.J., Lamb, J.R., Jennings, L.L., Aspelund, T., Emilsson, V., et al. (2022). A genome-wide association study of serum proteins reveals shared loci with common diseases. Nat. Commun. *13*, 480.
48. Tom, J., Chang, D., Wuster, A., Mukhyala, K., Cuenco, K., Cowgill, A., Vogel, J., Reeder, J., Yaspan, B., Hunkapiller, J., et al. (2019). Enabling genome-wide association testing with multiple diseases and no healthy controls. Gene *684*, 118–123.
49. Liang, Q., Dharmat, R., Owen, L., Shakoor, A., Li, Y., Kim, S., Vitale, A., Kim, I., Morgan, D., Liang, S., et al. (2019). Single-nuclei RNA-seq on human retinal tissue provides improved transcriptome profiling. Nat. Commun. *10*, 5743.
50. Reichenbach, A., and Bringmann, A. (2020). Glia of the human retina. Glia *68*, 768–796.
51. Mizutani, M., Gerhardinger, C., and Lorenzi, M. (1998). Müller cell changes in human diabetic retinopathy. Diabetes *47*, 445–449.
52. Okada, M., Matsumura, M., Ogino, N., and Honda, Y. (1990). Müller cells in detached human retina express glial fibrillary acidic protein and vimentin. Graefes Arch. Clin. Exp. Ophthalmol. *228*, 467–474.
53. Sarthy, V., and Egal, H. (1995). Transient induction of the glial intermediate filament protein gene in Müller cells in the mouse retina. DNA Cell Biol. *14*, 313–320.
54. Roesch, K., Stadler, M.B., and Cepko, C.L. (2012). Gene expression changes within Müller glial cells in retinitis pigmentosa. Mol. Vis. *18*, 1197–1214.
55. Fischer, A.J., Schmidt, M., Omar, G., and Reh, T.A. (2004). BMP4 and CNTF are neuroprotective and suppress damage-induced proliferation of Müller glia in the retina. Mol. Cell. Neurosci. *27*, 531–542.
56. Iribarne, M., Hyde, D.R., and Masai, I. (2019). TNFα induces Müller glia to transition from non-proliferative gliosis to a regenerative response in mutant Zebrafish presenting chronic photoreceptor degeneration. Front. Cell Dev. Biol. *7*, 296.
57. Dyer, M.A., and Cepko, C.L. (2000). Control of Müller glial cell proliferation and activation following retinal injury. Nat. Neurosci. *3*, 873–880.
58. Palazzo, I., Todd, L.J., Hoang, T.V., Reh, T.A., Blackshaw, S., and Fischer, A.J. (2022). NFkB-signaling promotes glial reactivity and suppresses Müller glia-mediated neuron regeneration in the mammalian retina. Glia *70*, 1380–1401.
59. Hoang, T., Wang, J., Boyd, P., Wang, F., Santiago, C., Jiang, L., Yoo, S., Lahne, M., Todd, L.J., Jia, M., et al. (2020). Gene regulatory networks controlling vertebrate retinal regeneration. Science *370*, eabb8598. https://doi.org/10.1126/science.abb8598.

60. Crabb, J.W., Miyagi, M., Gu, X., Shadrach, K., West, K.A., Sakaguchi, H., Kamei, M., Hasan, A., Yan, L., Rayborn, M.E., et al. (2002). Drusen proteome analysis: an approach to the etiology of age-related macular degeneration. Proc. Natl. Acad. Sci. USA *99*, 14682–14687.

61. Umeda, S., Suzuki, M.T., Okamoto, H., Ono, F., Mizota, A., Terao, K., Yoshikawa, Y., Tanaka, Y., and Iwata, T. (2005). Molecular composition of drusen and possible involvement of anti-retinal autoimmunity in two different forms of macular degeneration in cynomolgus monkey (Macaca fascicularis). FASEB J *19*, 1683–1685.

62. Chen, C.-Y., Melo, E., Jakob, P., Friedlein, A., Elsässer, B., Goettig, P., Kueppers, V., Delobel, F., Stucki, C., Dunkley, T., et al. (2018). N-Terminomics identifies HtrA1 cleavage of thrombospondin-1 with generation of a proangiogenic fragment in the polarized retinal pigment epithelial cell model of age-related macular degeneration. Matrix Biol. *70*, 84–101.

63. Tom, I., Pham, V.C., Katschke, K.J., Jr., Li, W., Liang, W.-C., Gutierrez, J., Ah Young, A., Figueroa, I., Eshghi, S.T., Lee, C.V., et al. (2020). Development of a therapeutic anti-HtrA1 antibody and the identification of DKK3 as a pharmacodynamic biomarker in geographic atrophy. Proc. Natl. Acad. Sci. USA *117*, 9952–9963.

64. Thee, E.F., Colijn, J.M., Cougnard-Grégoire, A., Meester-Smoor, M.A., Verzijden, T., Hoyng, C.B., Fauser, S., Hense, H.-W., Silva, R., Creuzot-Garcher, C., et al. (2022). The phenotypic course of age-related macular degeneration for ARMS2/HTRA1: the EYE-RISK consortium. Ophthalmology *129*, 752–764.

65. Kase, S., He, S., Sonoda, S., Kitamura, M., Spee, C., Wawrousek, E., Ryan, S.J., Kannan, R., and Hinton, D.R. (2010). alphaB-crystallin regulation of angiogenesis by modulation of VEGF. Blood *115*, 3398–3406.

66. Iwaki, T., Kume-Iwaki, A., Liem, R.K., and Goldman, J.E. (1989). Alpha B-crystallin is expressed in non-lenticular tissues and accumulates in Alexander's disease brain. Cell *57*, 71–78.

67. Liu, Y., Zhou, Q., Tang, M., Fu, N., Shao, W., Zhang, S., Yin, Y., Zeng, R., Wang, X., Hu, G., et al. (2015). Upregulation of alphaB-crystallin expression in the substantia nigra of patients with Parkinson's disease. Neurobiol. Aging *36*, 1686–1691.

68. Marino, M., Papa, S., Crippa, V., Nardo, G., Peviani, M., Cheroni, C., Trolese, M.C., Lauranzano, E., Bonetto, V., Poletti, A., et al. (2015). Differences in protein quality control correlate with phenotype variability in 2 mouse models of familial amyotrophic lateral sclerosis. Neurobiol. Aging *36*, 492–504.

69. van Noort, J.M., van Sechel, A.C., Bajramovic, J.J., el Ouagmiri, M., Polman, C.H., Lassmann, H., and Ravid, R. (1995). The small heat-shock protein alpha B-crystallin as candidate autoantigen in multiple sclerosis. Nature *375*, 798–801.

70. Dammer, E.B., Lee, A.K., Duong, D.M., Gearing, M., Lah, J.J., Levey, A.I., and Seyfried, N.T. (2015). Quantitative phosphoproteomics of Alzheimer's disease reveals cross-talk between kinases and small heat shock proteins. Proteomics *15*, 508–519.

71. Arac, A., Brownell, S.E., Rothbard, J.B., Chen, C., Ko, R.M., Pereira, M.P., Albers, G.W., Steinman, L., and Steinberg, G.K. (2011). Systemic augmentation of alphaB-crystallin provides therapeutic benefit twelve hours post-stroke onset via immune modulation. Proc. Natl. Acad. Sci. USA *108*, 13287–13292.

72. Ousman, S.S., Tomooka, B.H., van Noort, J.M., Wawrousek, E.F., O'Connor, K.C., Hafler, D.A., Sobel, R.A., Robinson, W.H., and Steinman, L. (2007). Protective and therapeutic role for alphaB-crystallin in autoimmune demyelination. Nature *448*, 474–479.

73. Shao, W., Zhang, S.-Z., Tang, M., Zhang, X.-H., Zhou, Z., Yin, Y.-Q., Zhou, Q.-B., Huang, Y.-Y., Liu, Y.-J., Wawrousek, E., et al. (2013). Suppression of neuroinflammation by astrocytic dopamine D2 receptors via αB-crystallin. Nature *494*, 90–94.

74. Dong, Z., Kase, S., Ando, R., Fukuhara, J., Saito, W., Kanda, A., Murata, M., Noda, K., and Ishida, S. (2012). Alphab-crystallin expression in epiretinal membrane of human proliferative diabetic retinopathy. Retina *32*, 1190–1196.

75. Bhagat, T.D., Chen, S., Bartenstein, M., Barlowe, A.T., Von Ahrens, D., Choudhary, G.S., Tivnan, P., Amin, E., Marcondes, A.M., Sanders, M.A., et al. (2017). Epigenetically aberrant stroma in MDS propagates disease via Wnt/β-catenin activation. Cancer Res. *77*, 4846–4857.

76. Ekström, E.J., Sherwood, V., and Andersson, T. (2011). Methylation and loss of Secreted Frizzled-Related Protein 3 enhances melanoma cell migration and invasion. PLoS One *6*, e18674.

77. Darr, O.A., Colacino, J.A., Tang, A.L., McHugh, J.B., Bellile, E.L., Bradford, C.R., Prince, M.P., Chepeha, D.B., Rozek, L.S., and Moyer, J.S. (2015). Epigenetic alterations in metastatic cutaneous carcinoma. Head Neck *37*, 994–1001.

78. Schlensog, M., Magnus, L., Heide, T., Eschenbruch, J., Steib, F., Tator, M., Kloten, V., Rose, M., Noetzel, E., Gaisa, N.T., et al. (2018). Epigenetic loss of putative tumor suppressor SFRP3 correlates with poor prognosis of lung adenocarcinoma patients. Epigenetics *13*, 214–227.

79. Marsit, C.J., Houseman, E.A., Christensen, B.C., Gagne, L., Wrensch, M.R., Nelson, H.H., Wiemels, J., Zheng, S., Wiencke, J.K., Andrew, A.S., et al. (2010). Identification of methylated genes associated with aggressive bladder cancer. PLoS One *5*, e12334.

80. Wang, Z., Liu, C.-H., Huang, S., and Chen, J. (2019). Wnt Signaling in vascular eye diseases. Prog. Retin. Eye Res. *70*, 110–133.

81. Chen, H.-C., Zhu, Y.-T., Chen, S.-Y., and Tseng, S.C.G. (2012). Wnt signaling induces epithelial-mesenchymal transition with proliferation in ARPE-19 cells upon loss of contact inhibition. Lab. Invest. *92*, 676–687.

82. Zhang, C., Su, L., Huang, L., and Song, Z.-Y. (2018). GSK3β inhibits epithelial-mesenchymal transition the Wnt/β-catenin and PI3K/Akt pathways. Int. J. Ophthalmol. *11*, 1120–1128.

83. Zhou, J., Jiang, J., Wang, S., and Xia, X. (2016). DKK1 inhibits proliferation and migration in human retinal pigment epithelial cells via the Wnt/β-catenin signaling pathway. Exp. Ther. Med. *12*, 859–863.

84. Umazume, K., Tsukahara, R., Liu, L., Fernandez de Castro, J.P., McDonald, K., Kaplan, H.J., and Tamiya, S. (2014). Role of retinal pigment epithelial cell β-catenin signaling in experimental proliferative vitreoretinopathy. Am. J. Pathol. *184*, 1419–1428.

85. Ishikawa, K., Sreekumar, P.G., Spee, C., Nazari, H., Zhu, D., Kannan, R., and Hinton, D.R. (2016). αB-Crystallin regulates subretinal fibrosis by modulation of epithelial-mesenchymal transition. Am. J. Pathol. *186*, 859–873.

86. Zhang, C., Barr, J.L., Owen, L.A., Shakoor, A., Vitale, A.T., Lillvis, J.H., Husami, N., Cromwell, P., Finley, R., Au, E., et al. (2022). Patterns of gene expression and allele-specific expression vary among macular tissues and clinical stages of Age-related Macular Degeneration. Preprint at bioRxiv. https://doi.org/10.1101/2022.12.19.521092.

87. Friedrich, U., Datta, S., Schubert, T., Plössl, K., Schneider, M., Grassmann, F., Fuchshofer, R., Tiefenbach, K.-J., Längst, G., and Weber, B.H.F. (2015). Synonymous variants in HTRA1 implicated in AMD susceptibility impair its capacity to regulate TGF-β signaling. Hum. Mol. Genet. *24*, 6361–6373.

88. Jacobo, S.M.P., Deangelis, M.M., Kim, I.K., and Kazlauskas, A. (2013). Age-related macular degeneration-associated silent polymorphisms in HtrA1 impair its ability to antagonize insulin-like growth factor 1. Mol. Cell Biol. *33*, 1976–1990.

89. Williams, B.L., Seager, N.A., Gardiner, J.D., Pappas, C.M., Cronin, M.C., Amat di San Filippo, C., Anstadt, R.A., Liu, J., Toso, M.A., Nichols, L., et al. (2021). Chromosome 10q26-driven age-related macular degeneration is associated with reduced levels of HTRA1 in human retinal pigment epithelium. Proc. Natl. Acad. Sci. USA *118*, e2103617118. https://doi.org/10.1073/pnas.2103617118.

90. Yang, Z., Camp, N.J., Sun, H., Tong, Z., Gibbs, D., Cameron, D.J., Chen, H., Zhao, Y., Pearson, E., Li, X., et al. (2006). A variant of the HTRA1 gene increases susceptibility to age-related macular degeneration. Science *314*, 992–993.

91. An, E., Sen, S., Park, S.K., Gordish-Dressman, H., and Hathout, Y. (2010). Identification of novel substrates for the serine protease HTRA1 in the human RPE secretome. Invest. Ophthalmol. Vis. Sci. *51*, 3379–3386.

92. Kanda, A., Stambolian, D., Chen, W., Curcio, C.A., Abecasis, G.R., and Swaroop, A. (2010). Age-related macular degeneration-associated variants at chromosome 10q26 do not significantly alter ARMS2 and HTRA1 transcript levels in the human retina. Mol. Vis. *16*, 1317–1323.

93. Melo, E., Oertle, P., Trepp, C., Meistermann, H., Burgoyne, T., Sborgi, L., Cabrera, A.C., Chen, C.-Y., Hoflack, J.-C., Kam-Thong, T., et al. (2018). HtrA1 mediated intracellular effects on tubulin using a polarized RPE disease model. EBioMedicine *27*, 258–274.

94. Jäger, M., Schubach, M., Zemojtel, T., Reinert, K., Church, D.M., and Robinson, P.N. (2016). Alternate-locus aware variant calling in whole genome sequencing. Genome Med. *8*, 130.

95. Li, H., and Durbin, R. (2009). Fast and accurate short read alignment with Burrows-Wheeler transform. Bioinformatics *25*, 1754–1760.

96. Van der Auwera, G.A., and O'Connor, B.D. (2020). Genomics in the Cloud: Using Docker, GATK, and WDL in Terra (O'Reilly Media, Inc.).

97. Gregoire Pau, J.R. (2017). HTSeqGenie (Bioconductor). https://doi.org/10.18129/B9.BIOC.HTSEQGENIE.

98. Adzhubei, I.A., Schmidt, S., Peshkin, L., Ramensky, V.E., Gerasimova, A., Bork, P., Kondrashov, A.S., and Sunyaev, S.R. (2010). A method and server for predicting damaging missense mutations. Nat. Methods *7*, 248–249.

99. Yu, G., Wang, L.-G., Han, Y., and He, Q.-Y. (2012). clusterProfiler: an R package for comparing biological themes among gene clusters. OMICS *16*, 284–287.

100. Robinson, M.D., McCarthy, D.J., and Smyth, G.K. (2010). edgeR: a Bioconductor package for differential expression analysis of digital gene expression data. Bioinformatics *26*, 139–140.

101. Aryee, M.J., Jaffe, A.E., Corrada-Bravo, H., Ladd-Acosta, C., Feinberg, A.P., Hansen, K.D., and Irizarry, R.A. (2014). Minfi: a flexible and comprehensive Bioconductor package for the analysis of Infinium DNA methylation microarrays. Bioinformatics *30*, 1363–1369.

102. Liberzon, A., Subramanian, A., Pinchback, R., Thorvaldsdóttir, H., Tamayo, P., and Mesirov, J.P. (2011). Molecular signatures database (MSigDB) 3.0. Bioinformatics *27*, 1739–1740.

103. Subramanian, A., Tamayo, P., Mootha, V.K., Mukherjee, S., Ebert, B.L., Gillette, M.A., Paulovich, A., Pomeroy, S.L., Golub, T.R., Lander, E.S., et al. (2005). Gene set enrichment analysis: a knowledge-based approach for interpreting genome-wide expression profiles. Proc. Natl. Acad. Sci. USA *102*, 15545–15550.

104. Phipson, B., Maksimovic, J., and Oshlack, A. (2016). missMethyl: an R package for analyzing data from Illumina's HumanMethylation450 platform. Bioinformatics *32*, 286–288.

105. McLean, C.Y., Bristor, D., Hiller, M., Clarke, S.L., Schaar, B.T., Lowe, C.B., Wenger, A.M., and Bejerano, G. (2010). GREAT improves functional interpretation of cis-regulatory regions. Nat. Biotechnol. *28*, 495–501.

106. Hao, Y., Hao, S., Andersen-Nissen, E., Mauck, W.M., 3rd, Zheng, S., Butler, A., Lee, M.J., Wilk, A.J., Darby, C., Zager, M., et al. (2021). Integrated analysis of multimodal single-cell data. Cell *184*, 3573–3587.e29.

107. McCarthy, D.J., Campbell, K.R., Lun, A.T.L., and Wills, Q.F. (2017). Scater: pre-processing, quality control, normalization and visualization of single-cell RNA-seq data in R. Bioinformatics *33*, 1179–1186.

108. Law, C.W., Chen, Y., Shi, W., and Smyth, G.K. (2014). voom: precision weights unlock linear model analysis tools for RNA-seq read counts. Genome Biol. *15*, R29.

109. Zhang, F., Flickinger, M., Taliun, S.A.G., InPSYght Psychiatric Genetics Consortium; Abecasis, G.R., Scott, L.J., McCaroll, S.A., Pato, C.N., Boehnke, M., and Kang, H.M. (2020). Ancestry-agnostic estimation of DNA sample contamination from sequence reads. Genome Res. *30*, 185–194.

110. Ferris, F.L., Davis, M.D., Clemons, T.E., Lee, L.-Y., Chew, E.Y., Lindblad, A.S., Milton, R.C., Bressler, S.B., and Klein, R.; Age-Related Eye Disease Study AREDS Research Group (2005). A simplified severity scale for age-related macular degeneration: AREDS Report No. 18. Arch. Ophthalmol. *123*, 1570–1574.

111. Krishnaswami, S.R., Grindberg, R.V., Novotny, M., Venepally, P., Lacar, B., Bhutani, K., Linker, S.B., Pham, S., Erwin, J.A., Miller, J.A., et al. (2016). Using single nuclei for RNA-seq to capture the transcriptome of postmortem neurons. Nat. Protoc. *11*, 499–524.

112. Ziffra, R.S., Kim, C.N., Ross, J.M., Wilfert, A., Turner, T.N., Haeussler, M., Casella, A.M., Przytycki, P.F., Keough, K.C., Shin, D., et al. (2021). Single-cell epigenomics reveals mechanisms of human cortical development. Nature *598*, 205–213.

113. Durinck, S., Stawiski, E.W., Pavía-Jiménez, A., Modrusan, Z., Kapur, P., Jaiswal, B.S., Zhang, N., Toffessi-Tcheuyap, V., Nguyen, T.T., Pahuja, K.B., et al. (2015). Spectrum of diverse genomic alterations define non–clear cell renal carcinoma subtypes. Nat. Genet. *47*, 13–21.

114. Wu, T.D., and Nacu, S. (2010). Fast and SNP-tolerant detection of complex variants and splicing in short reads. Bioinformatics *26*, 873–881.

115. van Dijk, D., Sharma, R., Nainys, J., Yim, K., Kathail, P., Carr, A.J., Burdziak, C., Moon, K.R., Chaffer, C.L., Pattabiraman, D., et al. (2018). Recovering gene interactions from single-cell data using data diffusion. Cell *174*, 716–729.e27.

116. Giambartolomei, C., Vukcevic, D., Schadt, E.E., Franke, L., Hingorani, A.D., Wallace, C., and Plagnol, V. (2014). Bayesian test for colocalisation between pairs of genetic association studies using summary statistics. PLoS Genet. *10*, e1004383.

117. Sudlow, C., Gallacher, J., Allen, N., Beral, V., Burton, P., Danesh, J., Downey, P., Elliott, P., Green, J., Landray, M., et al. (2015). UK biobank: an open access resource for identifying the causes of a wide range of complex diseases of middle and old age. PLoS Med. *12*, e1001779.

STAR★METHODS

KEY RESOURCES TABLE

REAGENT or RESOURCE	SOURCE	IDENTIFIER
Antibodies		
Mouse anti-human CD68	Dako	Cat# M0814
Rabbit anti-human CD117	Dako	Cat# A4502
Rabbit/mouse OmniMap-HRP	Ventana	Cat# 760-4647
Biological samples		
Human donor tissues	This paper	Table S1 ST1A Donor Statistics
Chemicals, peptides, and recombinant proteins		
1x cOmplete protease inhibitor with EDTA	Roche	Cat# 11836153001
Bluing Reagent	Ventana	Cat# 760-2037
Discovery Purple	Ventana	Cat# 760-229
DTT, molecular grade, 100uM	Promega	Cat# P1171
Hematoxylin II	Ventana	Cat# 790-2208
RNAlater	Ambion	Cat# AM7020
RNase inhibitor	Life Technologies	Cat# AM2682
RNAscope probe for human Hs-CLU	Advanced Cell Diagnostics	Cat# 606248
RNAscope probe for human Hs-CRYAB	Advanced Cell Diagnostics	Cat# 426278
SUPERase-In RNase inhibitor (20U/ul)	Life Technologies	Cat# AM2696
TRI Reagent solution	Thermo Fisher Scientific	Cat# AM9738
UltraPure BSA (50 mg/mL)	Life Technologies	Cat# AM2616
Ventana CC1	Ventana	Cat# 950-124
Critical commercial assays		
Agilent high sensitivity DNA kit	Agilent	Cat# 5067-4626
Chromium Single Cell 3′ GEM, Library and gel bead kit v3	10x Genomics	Cat# PN-100075
Chromium Single Cell ATAC Library & Gel bead kit, 16 reactions v1	10x Genomics	Cat# PN-1000110
EZ DNA methylation kit	Zymo research	Cat# D5001
Illumina HiSeq 2500 sequencing kit	Illumina	Cat# PE-402-4002, FC-402-4022
Illumina HiSeq 4000 sequencing kit	Illumina	Cat# PE-410-1001, GD-410-1001, FC-410-1002
Infinium Methylation EPIC-8+ v1.0 kit	Illumina	Cat# WG-317-1003
NEBNext rRNA depletion kit	New England Biolabs	Cat# E6310L
NovaSeq 6000 S2 flow cell	NovaSeq	Cat# 20028316
RNAscope 2.5 LSx Reagent kit-RED	ACDBio	Cat# 322750
SureSelect Strand-Specific RNA Library Prep	Agilent	Cat# G9691-90030
Deposited data		
Microscopy data	This paper	Mendeley Data: https://doi.org/10.17632/b4wb58tnwg.1
Processed counts data for bulk RNAseq, single-nucleus RNA-seq, single-nucleus ATAC-seq, and code	This paper	Zenodo Data: https://doi.org/10.5281/zenodo.7532115
Dimensionality reductions (UMAP) and processed count data to visualize single-nucleus RNA-seq	This paper	Single Cell Portal: SCP2012
Software and algorithms		
ASDPex	Jäger et al.[94]	https://doi.org/10.1186/s13073-016-0383-z
Biorender	www.biorender.com	

(*Continued on next page*)

Continued

REAGENT or RESOURCE	SOURCE	IDENTIFIER
BWA	Li and Durbin[95]	https://doi.org/10.1093/bioinformatics/btp324
cellranger version 3.1.0	www.10xgenomics.com	
cellranger-atac version 1.1.0	www.10xgenomics.com	
GATK version 0.7.9a-r786	Van der Auwera and O'Connor[96]	https://gatk.broadinstitute.org/
GENCODE	www.gencodegenes.org/human	GRCh38.p13
Geneious Prime 2022.1.1	www.geneious.com	
GenomeStudio 2.0	Illumina	
HTSeqGenie	Pau et al.[97]	https://doi.org/10.18129/B9.bioc.HTSeqGenie
PolyPhen	Adzhubei et al.[98]	https://doi.org/10.1038/nmeth0410-248
R package ArchR	Granja et al.[43]	https://doi.org/10.1038/s41588-021-00790-6
R package clusterProfiler	Yu et al.[99]	https://doi.org/10.1089/omi.2011.0118
R package edgeR	Robinson et al.[100]	https://doi.org/10.1093/bioinformatics/btp616
R package minfi	Aryee et al.[101]	https://doi.org/10.1093/bioinformatics/btu049
R package msigdb	Liberzon et al.[102]; Subramanian et al.[103]	https://doi.org/10.1093/bioinformatics/btr260; https://doi.org/10.1073/pnas.0506580102
R package missMethyl	Phipson et al.[104]	https://doi.org/10.1093/bioinformatics/btv560
R package rGREAT	McLean et al.[105]	https://doi.org/10.1038/nbt.1630
R package Seurat version 4	Hao et al.[106]	https://doi.org/10.1016/j.cell.2021.04.048
R package SCAVENGE	Yu et al.[41]	https://doi.org/10.1038/s41587-022-01341-y
R package scran	McCarthy et al.[107]	https://doi.org/10.1093/bioinformatics/btw777
R package vooom/limma	Law et al.[108]	https://doi.org/10.1186/gb-2014-15-2-r29
VerifyBamID	Zhang et al.[109]	https://doi.org/10.1101/gr.246934.118

RESOURCE AVAILABILITY

Lead contact

Requests for more information on the bulk data in the manuscript should be directed to Margaret M. DeAngelis (mmdeange@buffalo.edu). Requests for more information on the single-cell data should be directed to Luz Orozco (orozcogl@gene.com).

Materials availability

This study did not generate new unique reagents.

Data and code availability

The raw data reported in this study cannot be deposited in a public repository because of patient privacy reasons. To request access, please contact Yan Qi from Genentech's Legal department (qi.yan@gene.com) and/or the corresponding authors Margaret M. DeAngelis (mmdeange@buffalo.edu), Hsu-Hsin Chen (chen.hsuhsin@gene.com), Luz D. Orozco (orozcogl@gene.com).
Processed bulk methylation, bulk RNAseq, single-nucleus RNAseq, single-nucleus ATAC-seq data, and original code are available in Zenodo Data: https://doi.org/10.5281/zenodo.7532115.
Results from the single-nucleus RNAseq can be browsed on the Single Cell Portal, accession SCP2012.
Microscopy data reported in this paper are in Mendeley Data: https://doi.org/10.17632/b4wb58tnwg.1.
DOIs are listed in the key resources table.

EXPERIMENTAL MODEL AND SUBJECT DETAILS

De-identified human/patient details are listed in Table S1 ST1A. For the human donor eyes for bulk tissue analysis, institutional approval, and the consent of patients to donate their eyes for research purposes was obtained from the University of Utah and the University at Buffalo, and conformed to the tenets of the Declaration of Helsinki. All tissue was de-identified in accordance with HIPPA privacy rules.

The studies using human tissues for single-cell analysis and *in situ* hybridization were performed in accordance with FDA regulations and the Eye Bank Association of America (EBAA) medical standards regarding utilization of human tissue. Written, informed consent was obtained from all donors who provided human samples in accordance with the guidelines of the Declaration of Helsinki

for research involving the use of human tissue. The protocols for these studies were approved by the Pharma Repository Governance Committee at Genentech that serves as the Genentech/Roche Institutional Ethical Committee, to ensure that research on human samples stored in Genentech bio-repositories is performed in accordance with the subject's informed consent and with global ethical guidelines.

METHOD DETAILS

Human donor eyes for bulk tissue analysis

Methods for human donor eye collection were previously described in detail according to a standardized protocol.[2] Briefly, in collaboration with the Utah Lions Eye Bank, eyes used for this study were procured within a 6-hour post-mortem interval, defined as death-to-preservation time. Both eyes of the donor underwent post-mortem phenotyping with ocular imaging, including spectral domain optical coherence tomography (SD-OCT), and color fundus photography. Images were taken in a manner consistent with images utilized in the clinical setting. Dissections of donor eyes were carried out immediately to reliably isolate the RPE/choroid from the retina, and to separate the macula from the periphery. Isolated macula and peripheral RPE/choroid samples were then placed in cryotubes with the RNA stabilizing reagent RNAlater (Ambion, ThermoFisher, Waltham, MA, USA), stored at 4°C for 24 hours, and transferred to -80°C. To determine the precise ocular phenotype relative to disease and healthy aging, analysis of each set of images was performed by a team of retinal specialists and ophthalmologists at the University of Utah School of Medicine, Moran Eye Center, the Massachusetts Eye and Ear Infirmary Retina Service, and The Ross Eye Institute. Specifically, each donor eye was checked by an independent review of the color fundus and OCT imaging; discrepancies were resolved by collaboration between a minimum of three specialists to ensure a robust and rigorous phenotypic analysis. This diagnosis was then compared to medical records, and a standardized epidemiological questionnaire for the donor. For this study, both eyes for each donor were classified according to the modified Age Related Eye Disease Study Severity Grading Scale AREDS,[110] as previously described.[2] The tissues were predominantly from Caucasian ethnicity, one Hispanic, and two African American donors, from the Salt Lake City metropolitan area in Utah, USA. For the bulk RNAseq experiments, one eye was used for each donor for the majority of the donors, except both eyes were used for 3 donors which had discordant eyes. For the bulk DNA methylation experiments, one eye was used for each donor, except both eyes for one donor which had discordant eyes.

Bulk RNAseq

We profiled strand-specific total RNAseq, which included the complement of RNA transcripts beyond the polyadenylated subset. Macular and peripheral RPE/choroid samples were lysed with the TRI-Reagent solution (ThermoFisher Scientific, Waltham, MA), and total RNA was extracted from the aqueous phase of the lysate. Ribosomal RNA was depleted from total RNA preparations using the NEBNext rRNA Depletion kit (New England BioLabs Inc., Ipswich, MA) following manufacturer's protocols. 200 ng of ribo-depleted RNA was used for RNAseq library construction using the SureSelect Strand-Specific RNA Library Prep (Agilent). Multiplexed sequencing was performed at 11 libraries/lane on the Illumina HiSeq 4000 (Illumina Inc., San Diego, CA) with an average of 52 million reads per library.

DNA methylation microarray

Genomic DNA of the macular RPE/choroid samples was extracted from the interphase and the organic phase of the TRI-Reagent lysis (see above). On average, 780 ng of genomic DNA was bisulfite converted with the EZ DNA Methylation kit (Zymo Research) following the manufacturer's protocols. The bisulfite converted DNA samples were processed with Illumina's Infinium HD Methylation assay and hybridized to Illumina Methylation EPIC v1.0 850K arrays following the manufacturer's protocols. The arrays were scanned on the Illumina iScan instrument and visualized using Illumina's GenomeStudio software.

Human donor eyes for single-cell analyses and *in situ* hybridization

Post mortem human eyes were procured by the Florida Lion's Eye Institute for Transplantation and Research (Tampa, FL, USA). Clinical records and a family questionnaire were obtained for all donors.

Single-nucleus RNAseq (sNucSeq)

For the sNucSeq and snATAC-seq, one eye from each donor was used for sNucSeq and the contralateral eye was used for scATAC-seq. This approach captures nuclei from both the macula and the periphery. We performed sNucSeq from frozen whole globes as described by Orozco et al.,[10] using a modified protocol from Krishnaswami et al.[111] Briefly, eye cryosections midway from the posterior pole were used to assess overall RNA quality, and posterior cryosections estimated to contain the macula regions based on distance from the optic disc were lysed in ice cold Homogenization Buffer (250 mM sucrose, 25 mM KCl, 5 mM MgCl2, 10 mM Tris buffer pH 8.0, 1 mM dithiothreitol, 1X cOmplete™ protease inhibitors with EDTA (Roche), 0.1% v/v Triton X-100, 0.4 U/mL recombinant RNase Inhibitor (Ambion), 0.2 U/mL SUPERase-In (Ambion), 0.2 mg/ml DAPI) in a glass tissue homogenizer (Wheaton) and washed in the same buffer. Released nuclei with 2N DNA content were purified by fluorescence-activated cell sorting (BD-FACS-ARIA II) based on DAPI (4′,6-diamidino-2-phenylindole) and collected in 1% bovine serum albumin/1X RNAse-free phosphate buffered saline (Ambion) with 0.2 U/mL RNase Inhibitor (Ambion). Concentrated nuclei were counted on a Countess II (Life Technologies)

with Trypan Blue. The nuclei were immediately loaded onto 10X Chromium Single Cell 3' Expression v3 chips at 10K-20K nuclei per library. 2 libraries per donor were generated following the manufacturer's protocol. Libraries were sequenced using Illumina HiSeq 4000.

Single-nucleus ATACseq (snATAC-seq)

Matching regions of the contralateral eyes of the sNucSeq donors, including sclera, choroid, and retina, were used for single-nucleus ATAC-seq using the Chromium Single Cell ATAC v1 kits (10X Genomics). This approach captures nuclei from both the macula and the periphery. Nuclei were isolated following a modified protocol based on Ziffra et al.[112] Frozen sections were lysed in a glass tissue homogenizer (Wheaton) in an ice-cold homogenization buffer (see above) without DAPI and RNase inhibitors. Released nuclei were washed in ice-cold wash buffer (10 mM Tris buffer pH 7.4, 100 mM NaCl, 3 mM MgCl2, 0.1% Tween 20, 1% BSA), filtered through FlowMi cell strainers (70 μm and 40 μm, Bel-Art), counted and resuspended in 1X Diluted Nuclei Buffer (10X Genomics), and loaded onto 10X Chromium Chip E using ~15K nuclei per library. 2 libraries per donor were generated following the manufacturer's protocol. Libraries were sequenced using Illumina HiSeq 2500 and NovaSeq 6000 S2 flow cell.

Immunohistochemistry and RNAscope *in situ* hybridization

Formalin-fixed, paraffin-embedded (FFPE) donor eyes were sectioned transversely at 4 μm thickness throughout the entire macula, and every 30th section was stained with hematoxylin and eosin (H&E) to confirm the diagnosis of either healthy control, early/intermediate AMD, or geographic atrophy. Slides adjacent to those showing disease-defining features were used for immunohistochemistry using the Ventana Discovery XT platform, or *in situ* hybridization using the RNAScope platform.

For immunohistochemistry, FFPE sections were deparaffinized and heat antigen retrieved with Ventana CC1 at standard time (CC1std), followed by 25 μg/mL rabbit anti-human CD117 for 32 min. Signal was detected with Ventana Rabbit OmniMap-HRP incubation for 16 min, and labeled with Ventana Discovery Purple incubation for 16 min. Slides were counterstained with Ventana Hematoxylin II for 4 min, followed by Ventana Bluing Reagent for 4 min.

For *in situ* hybridization, sections were pretreated with RNAscope 2.5 LSx Protease for 30 min at ambient temperature. RNAscope probes from Advanced Cell Diagnostics targeting Hs-CRYAB or Hs-CLU were incubated for 120 min at 42°C and detected by RNAscope 2.5 LSx Reagent Kit-RED. In normal and iAMD eye sections, expression of both genes was largely absent in the outer nuclear layer (ONL) and inner and outer segments, and the *CRYAB* signal was absent from normal RPE. *CLU* ISH also showed punctate signals resembling cellular processes in the inner and outer plexiform layers and the GCL, and we observed strong staining in the apical portion of RPE cells. In the choroidal compartment, we found strong *CLU* expression in endothelial cells, and in non-pigmented cells with fibroblast morphology, with patterns largely similar between the control and disease groups. We observed increased expression of both genes in the INL and inner and outer segments in the perilesional regions in GA macular sections as compared to control and iAMD. For ISH, N=3 for each group: healthy control donors, iAMD donors, and GA donors. For IHC, control donors, N=4, iAMD donors, N=3 and GA donors, N=4.

QUANTIFICATION AND STATISTICAL ANALYSIS

Number of samples

The number of samples used for each of the analyses, their AREDS disease stage, PMI, sex, and age can be found in Table S1 ST1A Donor Statistics. Meta-data tables accompanying each dataset are included in the Zenodo repository. In summary:

For the DNA methylation microarrays from bulk macular RPE/choroid: the final data contained 83 samples from 39 normal controls, 29 early and intermediate AMD, and 15 GA samples, corresponding to 82 unique donors.

For the bulk RNAseq from macular RPE/choroid: the final data contained a total of 88 samples from 36 normal controls, 16 early AMD, 8 intermediate AMD, 10 GA, and 18 Neovascular AMD samples, corresponding to 85 unique human donors.

For the bulk RNAseq from peripheral RPE/choroid: the final data contained a total of 71 samples from 31 normal controls, 12 early AMD, 7 intermediate AMD, 7 GA, and 14 Neovascular AMD samples, corresponding to 70 unique human donors.

For the single-nucleus RNAseq from macular and peripheral retina, RPE, and choroid: the final data contained 164,399 cells, corresponding to 7 controls and 6 advanced AMD donors without phenotyping for disease stage.

For the single-nucleus ATACseq from macular and peripheral retina, RPE, and choroid: the final data contained 125,822 cells, corresponding to 7 controls and 5 advanced AMD donors without phenotyping for disease stage.

RNAseq in bulk RPE/choroid RNAseq from phenotyped donors

Differential expression analysis

Sequencing data analysis was performed as previously described.[113] Briefly, sequencing reads were mapped to the reference human genome (GRCh38), using the GSNAP short read aligner.[114] Transcript models used for differential expression were based on GENCODE Basic annotations. Expression counts per gene were quantified using *HTSeqGenie*.[97] We used *scran* to visualize expression counts as "logNormCounts" (Figures 1B, 5E, 5F, S5C). We used *edgeR*[100] to estimate size factors and normalize counts using TMM. We tested for differential gene expression between conditions of interest in our bulk RNAseq data using linear modeling with the voom/limma package[108] including "Sex" (categorical) and "Age" (numerical) as additional covariates, and adjusted *p*-values for

multiple genes tested using the Benjamini-Hochberg method. Genes were considered differentially expressed (DE) if they had adjusted p-value<0.05 and fold change>1.5 (in either direction). We performed the following DE comparisons: control vs early AMD (eAMD/AREDS2), control vs intermediate AMD (iAMD/AREDS3), control vs Geographic Atrophy AMD (GA), and control vs neovascular AMD (NEO). To identify genes changing in any of the dry AMD groups, we performed an additional analysis pooling dry AMD groups to increase statistical power: control vs eAMD + iAMD + GA (pooled dry AMD). To identify genes changing linearly with disease stage in dry AMD, we performed an analysis using the stage of dry AMD as a linear predictor using normal=1, eAMD=2, iAMD=3, and GA=4. To find DE genes changing with age independent of AMD, we modeled age as a linear predictor in the normal controls. We performed each of these contrasts in the macula or periphery regions of the eye (Figure S1A). Finally, we compared periphery vs macula across all groups. Notably, our sample sizes were larger for the macula samples (total n=88) than the periphery samples (total n=71).

Filtering out retina specific genes

Although special care was taken during dissection to reduce retinal contamination in the RPE/choroid collection, low levels of retina-specific expression in a subset of samples still contributed to artifacts in DE genes. To mitigate false positives due to retinal contamination, we filtered out 1,586 genes with significantly higher expression in the retina relative to the RPE/choroid (FDR<5% and 5-fold greater expression in the retina) by using our previously identified DE genes.[10]

Changes in cell composition

Since transcriptomic differences may reflect selective loss or enrichment of cell types in degenerative states, we tested potential changes in cellular composition between the disease states. We used a Wilcoxon Rank Sum Test to compare the distribution of fold expression differences between control and disease donors, using cell type marker gene sets for RPE, melanocytes, microglia, perivascular macrophages, and mesenchymal cells (Figure S1B). Overall, cellularity differences between the groups were lower than our expression fold-change cutoff at 1.5X, and hence are unlikely the main contributors to the top DE genes.

Pathway enrichment for bulk RNAseq

We performed pathway analysis for the DE comparison of normal vs pooled dry AMD in the macula. We used two approaches in the R package *clusterProfiler*[99]: Gene set enrichment analysis (GSEA),[103] and Over representation analysis (ORA). We obtained gene sets corresponding to Gene ontology biological process (GOBP), Gene Ontology Cellular Component (GOCC), and KEGG pathways, from the Molecular Signature (MSig) database using the package *msigdbr*.[102]

First, to perform the GSEA analysis, we sorted all the genes in the DE output based on the t-statistic in the descending order, with upregulated genes occurring at the top of the list. Second, we also performed pathway enrichments using ORA, which uses a hypergeometric test for the overlap between genes in the pathways and DE genes with FDR<5%. For both GSEA and ORA, we adjusted enrichment p-values for multiple hypothesis testing using the Benjamini-Hochberg method, and considered enrichment terms as significant if adjusted p-values values were less than 0.05.

GSEA identified pathways previously implicated in AMD, including lipid metabolism (adjusted p=0.002), epithelial cell proliferation (adjusted p=0.002), myeloid/leukocyte mediated immunity (adjusted p=0.01), regulation of immune response (adjusted p=0.02), macroautophagy (adjusted p=0.02), and response to TGF-beta (adjusted p=0.04). However, we did not find enriched pathways using the ORA approach with adjusted p-values less than 0.05.

DNA methylation in bulk RPE/choroid RNAseq from phenotyped donors

Initial processing and QC

We used the *minfi* package[101] in R to analyze the Illumina raw intensity data files (.idat). Methylation data was normalized using ''preprocessQuantile''. As part of the analysis pipeline, *minfi* uses control probes in the array to determine the background noise, and assigns a ''detection p-value'' to each observation. Observations with detection p-values>0.01 are considered to be failed. To QC the samples, we used the detection values to determine the percent of failed probes per sample, and the median absolute deviation to identify outliers. We found 13 outlier samples, where more than 5% of probes in those samples had a detection p-value>0.01. These outlier samples were removed from further analyses and can be visualized in the PCA (Figure S1D). This reduced our number of samples from 96 to 83. To QC the probes, we removed probes with a detection p-value>0.01 in 10% or more of the samples. In addition, probes with SNPs were removed using ''dropLociWithSnps''. This decreased the number of probes from 865,859 to 832,654. We used principal component analysis to evaluate possible batch effects, and we removed batch effects due to ''Sex'' and ''percent of failed probes'' using ''removeBatchEffect'' in *limma.* We used this QC'd data for subsequent analysis. Overall, the distribution of %methylation is comparable between disease groups, sex, microarray slides, and slide positions (Figure S1E). After excluding samples and probes that failed QC (Figure S1D), the final data contained 83 samples from 82 unique donors: 39 normal controls, 29 early and intermediate AMD (eAMD and iAMD), and 15 GA donor samples, from 832,654 probes.

Differential methylation analysis

We used ''dmpfinder'' to perform differential methylation analysis of individual CpG positions (DMPs). We used ''bumphunter'' to look for differentially methylated regions (DMRs). We performed differential methylation analysis on the following groups: (1) normal vs Geographic Atrophy AMD, (2) normal vs early/intermediate AMD (eAMD+iAMD), (3) normal vs all dry AMD (eAMD+iAMD+GA), (4) early/intermediate AMD vs GA. Multiple testing correction was performed in *minfi* using the False Discovery Rate (FDR) for DMPs, which were considered significant if FDR<5%. Uncertainty in Differentially Methylated Regions (DMRs) was assessed in *minfi* using the family-wise error rate (FWER) with 500 permutations, and DMRs were considered significant if the FWER was <5%. In a separate

analysis, we also attempted to remove invariant probes to minimize the number of tests performed; however this did not have an effect on the FWER. DMPs and DMRs were annotated for nearby genes using rGREAT,[105] and annotated to GRCh38 using the Illumina annotations for GRCh38.

Similar to the differential expression analysis, we also performed an analysis of DNA methylation using the stage of dry AMD as a linear predictor by encoding normal=1, early/intermediate AMD=3, and GA=4. We did not identify significant DMRs in the linear analysis, but we found one significant DMP in a CpG shore of the gene *SH3PXD2A*. This DMP was not previously identified in the pairwise analyses of DNA methylation.

Pathway enrichment for differential methylation

We performed ontology enrichment analysis using the *missMethyl* package in R.[104] We selected the top 500 DMPs from the control vs GA comparison as input to the "gometh" function, which tests all GO or KEGG terms. False discovery rates were calculated using the Benjamini and Hochberg method.[104] We did not identify enriched Gene Ontology or KEGG pathways among the top DMPs.

Relationship between differential methylation and expression

We evaluated potential effects of differentially methylated CpGs in three ways: (1) we examined DE of the nearest genes adjacent to DMPs annotated by rGREAT, (2) we used the peak-to-gene analysis in our sNucSeq and snATAC-seq data to identify genes regulated by chromatin regions overlapping the DMPs, and examined the DE statistics for the genes identified this way, and (3) we examined correlation between the bulk RNAseq and bulk DNA methylation levels, for genes identified based on proximity (1) or (2) peak-to-gene links. However, we note that only 19 donors overlapped both the bulk RNAseq and DNA methylation datasets (5 Normal, 9 eAMD/iAMD, and 5 GA), and hence our power to detect correlations using the 3rd approach is limited. For the third approach using the correlation between expression and DNA methylation, 4 genes showed a nominally significant correlation between expression and methylation: *AES* (Spearman rho=-0.54, p=0.02), *SAR1A* (Spearman rho=0.50, p=0.03), *CRYBG2* (Spearman rho=0.47, p=0.04), and *S1PR4* (Spearman rho=-0.48, pval=0.04). All 4 genes were identified through the peak-to-gene links, and only *AES* (aka *TLE5* and WNT pathway member) was also the nearest gene to a differentially methylated CpG.

Single-nucleus RNAseq (sNucSeq) analysis

To identify disease-related gene expression changes with cell type resolution, we generated sNucSeq libraries (10X Genomics) from Retina/RPE/choroid sections of 7 control and 6 AMD donor eyes as described above.[10]

Alignment

Single-nucleus RNAseq data were processed using *cellranger* from 10X Genomics (version 3.1.0). Since we used RNA derived from nuclei, both exonic and intronic reads were considered for downstream analysis by including introns in the pre-processing step of the human reference genome sequence (GRCh38). This algorithm outputs a count matrix of cells by genes, which we used for downstream analysis. We did not utilize the clustering and dimensionality reduction analysis that is output by *cellranger*.

Normalization, dimensionality reduction, cell clustering, and cluster markers

We performed downstream analysis using Seurat version 4.[106] We normalized UMIs using the "LogNormalize" method, and integrated the cells using CCA and "Sex" as the batching variable. We selected variable genes based on dispersion, then used these to compute principal components and UMAP dimensional reductions. We generated clusters of transcriptionally related cells, corresponding to cell types or cell subtypes, by using the graph-based clustering Louvain algorithm implemented in the Seurat function "FindClusters". The number of principal components we used to generate sample clusters varied from 4 to 30, depending on the cell type. We searched for cluster markers, i.e. gene expression markers that were more highly expressed in each cluster relative to all other clusters, using the "FindAllMarkers" function, based on the non-parametric Wilcoxon Rank Sum Test. Cluster marker genes were considered if they were expressed in at least 10% of the cells in the cluster, with a minimum difference of 30% in the fraction of cells expressing the marker between two clusters, and a minimum log2 fold change in expression of 0.25.

Quality control

While it is common practice to perform quality control (QC) of single-cell expression data by relying on hard thresholds for total UMIs, number of genes detected, and percentage of mitochondrial reads, we find that these arbitrary metrics can sometimes remove high quality cells, and/or fail to remove poor quality cells. For example, we routinely find that larger cells such as retinal ganglion cells are removed by QC using commonly used arbitrary thresholds for total UMI, since their larger size results in a greater amount of total RNA per cell. Instead, to perform QC, we used an iterative clustering approach. In this approach, we initially perform a "rough" clustering of cells, using a low number of principal components (e.g. 5 to 10) and low clustering resolution, into major cell types such as rods, cones, bipolar cells, etc. Then, for each major cell type, we perform sub-clustering of those cells with high resolution, with a high number of principal components (e.g. 20 to 30) and high clustering resolution. This results in a large number of clusters, where poor quality cells carrying high amounts of ambient RNA, low total UMI, or doublets, will cluster separately from the others due to large differences in their expression profiles. The poor quality clusters are identified by examining the expression of cell type marker genes, where we observe that poor quality clusters often express cell type markers that are specific to multiple cell types (for example from both rods and bipolar cells) and often express markers from the most abundant cell types in the experient, presumably due to ambient RNA contamination. We then remove poor quality clusters using "subset" in Seurat. This sub-clustering step can be done in an iterative manner to remove the majority of low quality cells, and is concluded with a final clustering analysis for cell subtypes in the given cell type. We repeated this process for each major cell type, which decreased the size of our data from 186,661 cells to 164,399 cells, and removed ~12% (22,262) of the original cells. This approach yielded QC'd cells and clusters with a high total number of

UMIs and number of genes detected, and low percentage of mitochondrial reads (Figures S2A–S2C). The proportion of each major cell type in control vs. AMD donors is shown in (Figure S2D) where we observed a reduction in the percent of RPE cells in AMD donors. However, we observed substantial variability, possibly due to experimental and donor variability, as well as a relatively small sample size in control (N=7) and AMD donors (N=6).

Pseudo-bulk differential expression analysis

Pseudo-bulk data were derived from our sNucSeq data by aggregating the cells of each sample of the same cell type using ''aggregateAcrossCells'' using *scran* as described.[107] For n donors and m cell types, it creates n*m total possible pseudo-bulks, which are aggregates of cells of a given cell type from a single donor. We used *scran* to visualize the resulting pseudo-bulk counts as ''logNormCounts'' (Figures 3E, 3F and S3A–S3E). To perform differential expression analysis (DE), we used *edgeR* to estimate size factors and normalize counts using TMM.[100] Differential expression was performed on this data to compare control versus AMD samples, for each cell type, using the voom/limma method for bulk RNAseq as described above. We included ''Sex'' (categorical) as an additional covariate in the linear model. Pseudo-bulk samples were considered for DE analysis if the number of cells used to generate donor-cell type pseudo-bulk was at least 10. Genes were considered for analysis if they were (1) protein-coding genes or lincRNAs, and (2) if they were expressed with normalized log counts>5, in at least 10% of samples, in either retina or RPE/choroid bulk RNAseq datasets published by our group,[10] which restricted the analysis to 18,981 features. Results from this pseudo-bulk differential expression analysis can be found in Table S1 ST1G.

Pathway enrichment for differential expression in sNucSeq

For each major cell type, we performed pathway enrichments for pseudobulk DE in sNucSeq using the same approach as for DE in bulk RNAseq, as described above. While there were not enough genes DE with FDR<5% to perform pathway enrichment using ORA, GSEA identified several pathways implicated in AMD, such as lipid oxidation in RPE (adjusted p=1.4E-03), regulation of cell adhesion mediated by cadherin in RPE (adjusted p=0.02), ion homeostasis in Müller glia (adjusted p=3.6E-03), regeneration in Müller glia (adjusted p=0.02), and aging in Fibroblasts (adjusted p=0.04).

Müller glia shift

To compare proportion of AMD cells across the Müller glia clusters (Muller 1, Muller 2, and Muller 3), we performed a Fisher's exact test, where the number of successes equaled the number of AMD cells of a given cluster, and the number of failures was the total number of cells in the cluster minus the number of successes. This approach revealed a statistically significant difference in the proportion of AMD cells across the Müller clusters with Fisher's Exact p-value=5.0E-04.

Single-nucleus ATAC-seq (snATAC-seq)

Alignment

Single-nuclei ATACseq data were processed using *cellranger-atac* from 10X Genomics (version 1.1.0), where reads were aligned to the human reference genome sequence (GRCh38). This algorithm outputs a count matrix of fragments, which we used for downstream analysis and calling of peaks. We did not utilize the peak calling, clustering, or dimensionality reduction analysis that is output by *cellranger-atac*.

Normalization, dimensionality reduction, cell clustering, marker peaks, peak calling

We used the ArchR package[43] to analyze the snATAC-seq data. We filtered the data using Transcription Start Site Enrichment (TSS) >4 and a minimum number of 1,000 fragments for analysis. Dimensionality reduction was performed using Latent Semantic Indexing (LSI) using the tile matrix created and ''addIterativeLSI'', followed by UMAP dimensionality reduction using ''addUMAP''. We clustered cells based on the Louvain algorithm, which is implemented in ArchR using ''addClusters''. Gene accessibility ''Gene scores'' were estimated based on a weighted distance to the start site of each gene, and imputed using MAGIC[115] as implemented in ArchR. We identified cluster marker genes based on ATAC accessibility using the Wilcoxon Rank Sum Test in ''getMarkerFeatures'', and we utilized the accessibility cluster marker genes to assign cell type labels to each cluster. We called peaks for each cell type using MACS2 in ArchR. We repeated this process by sub-clustering each major cell type, which improved our resolution to identify cell subtypes, and allowed us to further remove clusters composed of low quality cells. Overall, QC analysis decreased our raw cell number from 188,122 to 125,822, removing ~33% of cells.

Integration of ATAC and RNA

Since our snATAC-seq and sNucSeq were performed separately, we used Canonical Correlation Analysis (CCA) implemented in ArchR to integrate our two data types, which utilized the accessibility gene scores (in the snATAC-seq) and expression levels (sNucSeq) to find the cells most similar to each other. We also used CCA integration to transfer cell type labels between our expression and ATAC data, and found the cell type labels were consistent with our assignments based on cell type marker genes. Representative cell type specific marker accessibility, and expression based on CCA integration, are shown in Figures 4E and 4F.

Pseudo-bulk differential peak analysis

Pseudo-bulk data were derived from our snATAC-seq data by aggregating the cells of each sample of the same cell type using ''aggregateAcrossCells'' using *scran*[107] as described above. To perform differential peak analysis, we used *edgeR* to estimate size factors and normalize the resulting pseudo-bulk count matrix using TMM.[100] In contrast to the sNucSeq, we used the ''Peak'' matrix generated by MACS2 in ArchR as the input matrix to compute pseudo-bulks. Differential peak accessibility was performed on this data to compare control versus AMD samples, for each cell type, using the voom-limma method as described above. We included ''Sex'' as an additional covariate in the linear model.

Single-cell enrichments for AMD GWAS loci

SCAVENGE

We identified disease relevant cell types using *SCAVENGE* in conjunction with our snATAC-seq data, and GWAS loci for AMD. We performed fine mapping of the AMD consortia GWAS loci[6] using *coloc*[116] with minor allele frequencies from the UK BioBank.[117] We used these fine mapping results and snATAC-seq from all major cell types in the retina, RPE, and choroid as inputs for *SCAVENGE* as described,[41] which assigned a trait relevance score (TRS) to each cell type. We identified significant cell type enrichments with empirical FDR<5% based on 1,000 permutations.

Peak to gene links

We performed correlation of chromatin accessibility peaks and gene expression across all major cell types using our integrated snATAC-seq and sNucSeq datasets using ArchR as described by the authors. This identified putative regulatory relationships, or ''peak-to-gene links'', between accessible peaks and genes. We considered peak-to-gene links as significant if the Pearson's correlation R>0.3 and FDR<5%. To prioritize putative causal genes for AMD, we identified peak-to-gene links in chromatin regions overlapping published GWAS loci for risk of AMD.[6,7,28,31–39] Results of this analysis are in Table 2.

Rare variant burden test

Study population

We performed a whole-genome sequencing study using DNA derived from blood samples obtained from patients with GA participating in clinical trials for Lampalizumab: NCT01229215 (MAHALO), NCT02247479 (CHROMA), NCT02247531 (SPECTRI) and NCT02479386 (PROXIMA A/B). These study populations were selected for inclusion on the basis of available phenotypic information and DNA availability for whole-genome sequencing. Samples and data for controls without GA were obtained from clinical trial studies of asthma, cancer, chronic obstructive pulmonary disease, inflammatory bowel disease, idiopathic pulmonary fibrosis and rheumatoid arthritis. All patients included in this study provided written informed consent for whole-genome sequencing or array genotyping of their DNA. Ethical approval was provided as per the original clinical trials.

DNA analysis

The whole-genome sequencing data was generated to a read depth of 30X using the HiSeq platform (Illumina X10, San Diego, CA, USA) processed using the Burrows-Wheeler Aligner (BWA),[95] and Genome Analysis Toolkit (GATK)[96] best practices pipeline. Whole genome sequencing short reads were mapped to GRCh38 (GCA_000001405.15), including alternate assemblies, using BWA version 0.7.9a-r786 to generate BAM files. All sequencing data was subject to quality control and was checked for concordance with SNP fingerprint data collected before sequencing. After filtering for genotypes with a GATK genotype quality greater than 90, samples with heterozygote concordance with SNP chip data of less than 75% were removed. Sample contamination was determined with VerifyBamID[109] software, and samples with a freemix parameter of more than 0.03 were excluded. Joint variant calling was done using the GATK best practices joint genotyping pipeline to generate a single variant call format (VCF) file. The called variants were then processed using ASDPEx[94] to filter out spurious variant calls in the alternate regions.

Quality control

Samples were then excluded if the call rate was less than 90%. Identity by descent analysis was used to detect and filter out relatedness in our data; samples were excluded if PI_HAT was 0.4 or higher. Samples were removed if they showed excess heterozygosity with more than three Standard Deviations from the mean. This resulted in 1,707 cases and 2,611 controls. Sample genotypes were set to missing if the Genotype Quality score was less than 20 and SNPs were removed if the missingness was higher than 5%. SNPs were filtered if the significance level for the Hardy-Weinberg equilibrium test was less than $5x10^{-8}$. The allele depth balance test was performed to test for equal allele depth at heterozygote carriers using a binomial test; SNPs were excluded if the p-value was less than $1x10^{-5}$.

Statistical analysis

A rare-variant (MAF<1%) gene burden test was performed using exonic SNPs, comparing the number of individuals carrying a variant in a gene in the case-case sub-phenotypes. The rare-variant gene burden test was performed in R using the CMC Wald test. Rare variants were included if they had a HIGH impact score (frameshift, stop gain, splice acceptor, etc) or a MODERATE impact score (missense, splice sites, and insertions or deletions). Three different burden tests were performed: 1) all MODERATE and HIGH impact variants, 2) HIGH impact variants and MODERATE impact variants predicted to be damaging in PolyPhen[98] and 3) HIGH impact variants.

Due to the use of samples from non-ophthalmic diseases as controls since healthy controls were not readily available, we used a genotype-on-phenotype reverse regression to remove non-AMD specific findings.[48] Associations were flagged and removed if they were driven by diseases other than GA.

Phylogenetic tree

We constructed a phylogenetic tree for the *C6orf223* RNA in the Geneious Tree builder, using the Tamura-Nei genetic distance model, and the Neighbor-joining model to build the tree, with no outgroup. We used the Refseq transcripts for Human (NR_160954.1), Baboon (XM_045390971), Chimpanzee (XM_003950854), Marmoset (XM_035297792), crab-eating Macaque (XM_045390971), large flying fox (XM_023527689), Orca (XM_033424347), and Pig (XM_021100037), and aligned them in Geneious prime 2022.1.1 using MAFFT alignment v. 7.450 and default parameters (auto algorithm, 200 PAM, k=2 scoring matrix, gap open penalty 1.53, offset value 0.123).